



# HHS Public Access

## Author manuscript

*Cell Rep.* Author manuscript; available in PMC 2024 February 09.

Author Manuscript

Author Manuscript

Author Manuscript

Author Manuscript

Published in final edited form as:

*Cell Rep.* 2023 January 31; 42(1): 111942. doi:10.1016/j.celrep.2022.111942.

## Mutations in the transcriptional regulator MeCP2 severely impact key cellular and molecular signatures of human astrocytes during maturation

Jialin Sun<sup>1</sup>, Sivan Osenberg<sup>1,2,3</sup>, Austin Irwin<sup>1</sup>, Li-Hua Ma<sup>3,4</sup>, Nigel Lee<sup>2,3</sup>, Yangfei Xiang<sup>6</sup>, Feng Li<sup>4,7</sup>, Ying-Wooi Wan<sup>3,5</sup>, In-Hyun Park<sup>6</sup>, Mirjana Maletić-Savatic<sup>2,3,\*</sup>, Nurit Ballas<sup>1,8,\*</sup>

<sup>1</sup>Department of Biochemistry and Cell Biology, Stony Brook University, Stony Brook, NY 11794, USA

<sup>2</sup>Departments of Pediatrics-Neurology, Baylor College of Medicine, Houston, TX 77030, USA

<sup>3</sup>Jan and Dan Duncan Neurological Research Institute at Texas Children's Hospital, Houston, TX 77030, USA

<sup>4</sup>Advanced Technology Cores, Baylor College of Medicine, Houston, TX 77030, USA

<sup>5</sup>Department of Molecular and Human Genetics, Baylor College of Medicine, Houston, TX 77030, USA

<sup>6</sup>Department of Genetics, Yale Stem Cell Center, Yale School of Medicine, New Haven, CT 06520, USA

<sup>7</sup>Center for Drug Discovery and Department of Pathology & Immunology, Baylor College of Medicine, Houston, TX 77030, USA

<sup>8</sup>Lead contact

## SUMMARY

Mutations in the *MECP2* gene underlie a spectrum of neurodevelopmental disorders, most commonly Rett syndrome (RTT). We ask whether *MECP2* mutations interfere with human astrocyte developmental maturation, thereby affecting their ability to support neurons. Using human-based models, we show that RTT-causing *MECP2* mutations greatly impact the key role of astrocytes in regulating overall brain bioenergetics and that these metabolic aberrations are likely mediated by dysfunctional mitochondria. During post-natal maturation, astrocytes rely on neurons to induce their complex stellate morphology and transcriptional changes. While *MECP2* mutations cause cell-intrinsic aberrations in the astrocyte transcriptional landscape, surprisingly, they do not

\*Correspondence: maletics@bcm.edu (M.M.-S.), nurit.ballas@stonybrook.edu (N.B.).

### AUTHOR CONTRIBUTIONS

J.S., S.O., M.M.S., and N.B. designed the research. J.S., S.O., A.I., L.H.M., Y.X., and F.L., performed research. J.S., S.O., L.H.M., F.L., M.M.S., and N.B. analyzed the data. J.S., S.O., N.L., and Y.W.W. performed bioinformatics analysis. Y.X. and I.H.P. generated the human stem cell lines. J.S., S.O., M.M.S., and N.B. wrote the paper with contribution by all authors. N.B. directed the overall research.

### DECLARATION OF INTERESTS

The authors declare no competing interests.

### SUPPLEMENTAL INFORMATION

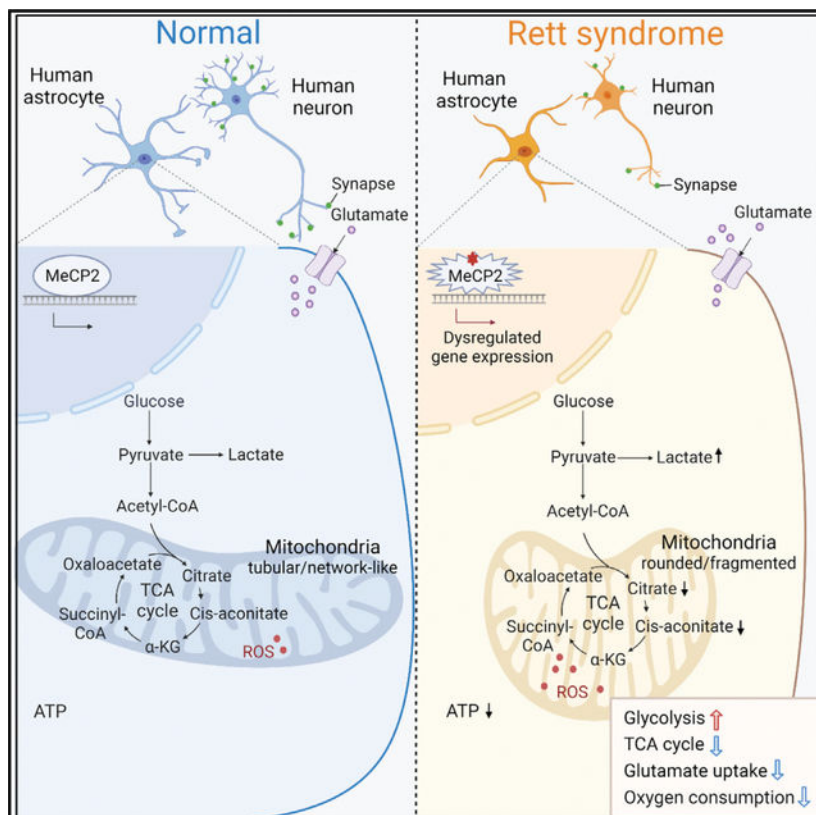
Supplemental information can be found online at <https://doi.org/10.1016/j.celrep.2022.111942>.

affect the neuron-induced astrocyte gene expression. Notably, however, astrocytes are unable to develop complex mature morphology due to cell- and non-cell-autonomous aberrations caused by *MECP2* mutations. Thus, *MECP2* mutations critically impact key cellular and molecular features of human astrocytes and, hence, their ability to interact and support the structural and functional maturation of neurons.

### In brief

Sun et al. show that Rett syndrome-causing mutations in MeCP2 impair the gene expression landscape of human astrocytes, including genes associated with astrocyte development, and negatively affect their structural maturation and energy metabolism, mediated by dysfunctional mitochondria. These together negatively impact the astrocyte's key role in supporting neurons.

### Graphical Abstract



### INTRODUCTION

Mutations in the X-linked gene *MECP2* cause a variety of neuropsychiatric disorders,<sup>1–4</sup> including Rett syndrome (RTT), a severe post-natal neurodevelopmental disorder characterized by progressive loss of motor, verbal, cognitive, and social skills, and the development of breathing abnormalities, seizures, tremors, and stereotypies.<sup>3,4</sup> Initially, RTT was attributed solely to neuronal dysfunction, but more recent studies have challenged

this view and suggested that glia, in particular astrocytes, are an integral part of the RTT neuropathology.<sup>5–9</sup>

Despite these exciting advances, there remain major obstacles to understanding the mechanisms that underlie RTT. One is that the disease phenotype in RTT patients is more severe than in mouse models, suggesting that *MECP2* mutations affect neurons and glia differently in humans and mice. In support of this view, human astrocytes are by far larger and more structurally complex than mouse astrocytes and have a different transcriptional landscape.<sup>10–12</sup> Also, and particularly relevant to MeCP2 as a gene regulator, only 30% of human astrocyte-enriched genes are enriched in mouse astrocytes.<sup>11–13</sup> Furthermore, recent studies report major differences between human and mouse astrocytes in mitochondrial physiology, energy metabolism, and susceptibility to oxidative stress and hypoxia.<sup>14</sup> Thus, to understand how disease-causing mutations affect human brain cells, given these striking cellular and molecular disparities, it is critical to use human-based models of RTT.

During post-natal brain development, astrocytes depend on neurons to induce their complex stellate morphology and elicit transcriptional changes that accompany this structural transformation.<sup>15–17</sup> The mature structural complexity and gene expression induced by neurons are fundamental to the astrocyte functions on which neurons critically depend, including for metabolic and neurotrophic support, neurotransmitter uptake and recycling, synaptogenesis, and plasticity.<sup>18</sup> Yet, it remains unknown how *MECP2* mutations in neurons and/or astrocytes affect astrocyte maturation.

We hypothesized that RTT-causing *MECP2* mutations in the developing human brain affect key cellular and molecular properties of astrocytes during their maturation and, thereby, their support to neurons. To test this hypothesis, we used several human pluripotent stem cell (hPSC)-based platforms to model astrocyte developmental maturation *in vitro* and *in vivo*. Here, we show that many genes, including key human astrocyte-enriched genes, are aberrantly expressed in mutant astrocytes due to cell-intrinsic defects in gene expression. Importantly, we show that metabolic homeostasis, including energy and glutamate metabolism, and redox balance, is significantly impaired in mutant human astrocytes and that dysfunctional mitochondria likely lie at the heart of these metabolic abnormalities. We further show that during astrocyte developmental maturation, the *MECP2* mutations exerted dramatic effects on astrocyte stellate morphology due to cell- and non-cell-autonomous defects in mutant astrocytes and neurons, yet had no effect on neuron-induced astrocyte gene expression. Finally, we demonstrate that the aberrations caused by *MECP2* mutations in human astrocytes and/or neurons severely impact the structural plasticity of neurons.

## RESULTS

### RTT-causing *MECP2* mutations do not affect astrocyte differentiation from hPSCs

To avoid potential confounders stemming from complex RTT genetics and reprogramming of induced pluripotent stem cells, and from unstable X-inactivation that often occurs during culturing of female hPSCs,<sup>19–22</sup> we used male human embryonic stem cells (hESCs) to generate our human-based models. We inserted the R270X (C808T) and R133C (C397T)

Author Manuscript  
Author Manuscript  
Author Manuscript  
Author Manuscript

mutations via CRISPR/Cas9 technology<sup>23</sup> (Figure 1A). The mutant hESC-lines maintained pluripotency and normal karyotypes like their isogenic wild-type (WT) controls (Figure S1). We chose these two mutations because both occur frequently in RTT patients.<sup>24</sup>

However, the R270X mutation manifests in more severe clinical phenotypes than the R133C mutation<sup>25,26</sup>; therefore, we focused our study on R270X while comparing the effect of R133C in selected experiments.

To investigate the cell-autonomous effects of the *MECP2* mutations, we first differentiated the mutant and WT hESCs into forebrain astrocytes in a monolayer culture (monoculture) (Figure 1B). The hESCs harboring the R270X or R133C mutation differentiated into neuroprogenitor cells (NPCs) (Figures 1C, S2A, and S2B) and then into astrocyte progenitor cells (APCs) (Figures 1D, 1E, and S2C), based on the expression of the respective NPC and APC markers, with high and similar efficiency as their isogenic WT controls. To obtain a more homogeneous population of APCs for subsequent differentiation into astrocytes, we sorted them for high expressors of the surface marker CD44.<sup>27</sup> While most (approximately 80%) WT and mutant APC cells were CD44 positive before sorting, nearly all APCs (>98%) were CD44 positive after sorting and expressed SOX9, an astrocyte lineage-specific nuclear marker<sup>28</sup> (Figure 1E). Consistent with previous reports,<sup>11,29</sup> the CD44 and SOX9 levels decreased as APCs differentiated into astrocytes, with no significant differences between mutant and WT APCs or between mutant and WT astrocytes (Figure 1E). Like WT astrocytes, nearly all mutant astrocytes were positive for S100B and glial fibrillary acidic protein (GFAP) (Figures 1F and S2D). We also analyzed cell proliferation and found that in both WT and mutant APC cultures, approximately 50% of the cells were positive for the cell proliferation marker Ki67, while in both WT and mutant astrocyte cultures, only 2%–3% of cells were Ki67 positive (Figure S2E). Finally, we found no significant differences in the expression of several markers present in reactive astrocytes<sup>30</sup> between mutant and WT astrocytes (Figures 1F–1H), suggesting that *MECP2* mutations do not lead to human astrocyte pro-reactive state.

### Human astrocytes carrying RTT-causing *MECP2* mutations differentially express numerous genes associated with key cellular pathways

To determine whether *MECP2* mutations alter the intrinsic properties of human astrocytes cell-autonomously, we first examined the gene expression profiles of WT and R270X mutant astrocytes in monoculture. RNA sequencing (RNA-seq) analysis showed that, of the approximately 18,000 identified genes, 1,621 were dysregulated (fold change of >1.5-fold;  $p_{adj} < 0.05$ ) in mutant astrocytes (Table S1). Of the dysregulated genes, more were up-regulated than down-regulated (967 vs. 654, respectively) (Figure 2A; Table S1). Gene ontology (GO) and Kyoto Encyclopedia of Genes and Genomes (KEGG) pathway analyses revealed significant enrichment in various signaling pathways, several of which related to cell morphology and energy metabolism (Figure 2B).

We then asked how the *MECP2* mutation in human astrocytes affects the cell-autonomous expression of two astrocyte-enriched gene sets normally expressed at different maturation stages<sup>11</sup>: (1) fetal astrocyte-enriched genes, expressed preferentially in the immature astrocytes of the fetal human brain, and (2) mature astrocyte-enriched genes, expressed

Author Manuscript  
Author Manuscript  
Author Manuscript  
Author Manuscript

preferentially in the post-natal astrocytes of the juvenile and adult human brains, many of which are induced to high levels upon interaction with neurons<sup>16</sup> and are fundamental for neuron support. We first evaluated the state of astrocyte maturation in monoculture by analyzing the expression levels of these two gene sets. We found that 52% and 48% of fetal and 35% and 38% of mature gene sets expressed (>300 normalized read counts) in WT and mutant astrocytes, respectively, with a very high similarity between the specific genes expressed in WT and mutant astrocytes. These data suggest that both WT and mutant astrocytes that exited the cell cycle (Figure S2E) are in transition from fetal to mature stage. We then analyzed whether fetal and/or mature genes are differentially expressed in mutant versus WT astrocytes and found 68 fetal and 64 mature astrocyte-enriched genes dysregulated in mutant astrocytes (Figure 2C; Table S2). Gene set enrichment analysis indicated significantly more up-regulated than down-regulated mature astrocyte-enriched genes in mutant astrocytes (Figure 2D right). Quantitative reverse transcriptase PCR validated several differentially expressed mature astrocyte-enriched genes involved in key functions and cellular pathways, such as the up-regulation of *TGFB2* involved in synapse formation and elimination and the down-regulation of *SLC1A3*, encoding the astrocyte excitatory glutamate transporter 1 (EAAT1) (Figure 2E). Importantly, we found that, of the 11 dysregulated genes we validated (Figure 2E), 8 were dysregulated also in R133C mutant astrocytes (Figure S2F), while only 3 that were dysregulated in R270X astrocytes remained unchanged in R133C astrocytes. Notably, none of the genes tested in the R133C-mutant astrocytes exhibited dysregulation opposite of that observed for the same genes in the R270X-mutant astrocytes. Furthermore, the dysregulated genes were more severely dysregulated in R270X compared with R133C astrocytes, consistent with the more severe clinical phenotype of RTT patients with the R270X mutation. These results suggest that different *MECP2* mutations cause similar types of transcriptome aberrations, albeit with different severities.

### **Human astrocytes with *MECP2* mutations have impaired energy metabolism, redox balance, and glutamate homeostasis, mediated by dysfunctional mitochondria**

Astrocytes are the key regulators of brain bioenergetics and neurons depend on them for a variety of metabolic processes, including energy metabolism and neurotransmitter homeostasis.<sup>31–34</sup> Several previous studies suggested impaired metabolism and mitochondria in RTT,<sup>21,35–38</sup> but whether astrocytes, in particular human astrocytes with *MECP2* mutations, have impaired energy metabolism remains unknown. Because several GO terms suggest an aberrant expression of genes involved in energy metabolism (Figure 2B), we reasoned that those metabolic processes might be altered in mutant human astrocytes.

We first examined the extracellular metabolites: those that astrocytes secrete into or uptake from the culturing media. Untargeted <sup>1</sup>H nuclear magnetic resonance (NMR) analyses of mutant (R270X and R133C) and WT astrocyte-conditioned media (ACM) revealed that both R270X- and R133C-mutant ACM had significantly higher lactate and lower pyruvate levels (Figures 3A and S3A–S3C), suggesting that mutant astrocytes secrete more lactate while they uptake more pyruvate from the media and/or secrete less of it. These metabolites are energy substrates; pyruvate is converted to lactate during the last step of anaerobic

Author Manuscript  
Author Manuscript  
Author Manuscript  
Author Manuscript

glycolysis.<sup>39,40</sup> Untargeted liquid chromatography-mass spectrometry (LC-MS) analyses (Figures S3D and S3G) showed that mutant astrocytes secreted significantly less succinate (Figures S3E and S3F), a tricarboxylic acid (TCA) cycle intermediate (Figure 3C), and much more (12-fold) palmitoyl-sn-glycero-3-phosphocholine (LPC) than WT astrocytes (Figures S3H and S3I). Interestingly, LPC production increases when the hypoxia-inducible factor 1-phospholipase A2 group 16 (PLA2G16) axis is up-regulated,<sup>41,42</sup> consistent with our RNA-seq data (Figure S3J). The elevated lactate and LPC and the reduced pyruvate and succinate point to alterations in bioenergetics and further suggest that mutant astrocytes are in an anaerobic or hypoxic-like state.

We, therefore, examined the intracellular metabolome of mutant astrocytes. Untargeted <sup>1</sup>H NMR identified 15 metabolites at significantly higher levels in mutant astrocytes, including amino acids and glycolysis intermediates (Figures 3B and S3K). Notably, lactate was 2.5-fold higher in mutant astrocytes, suggesting they both produce and secrete more lactate than WT astrocytes. While the intracellular level of pyruvate was similar between mutant and WT astrocytes, lactate, alanine, and acetate—all three produced from pyruvate—were significantly higher in mutant astrocytes (Figures 3B and 3C left). This may explain the higher pyruvate demand and consumption indicated by its reduced levels in the mutant ACM (Figures 3A and S3C). In contrast, targeted LC-MS/MS showed lower levels of several TCA cycle intermediates in mutant astrocytes, particularly citrate, a key metabolite in the entry point to the TCA cycle (Figure 3C right). We also found a significantly decreased level of cellular adenosine triphosphate (ATP) (Figure 3D) in mutant astrocytes. Interestingly, our RNA-seq data-based KEGG glycolytic pathway analysis revealed a significant up-regulation of many genes that encode glycolytic enzymes (Table S3). Additionally, the glucose transporter genes (*SLC2A12*, *SLC2A3*, *SLC2A10*) were expressed at higher levels in mutant astrocytes (Table S1). These data together suggest that mutant astrocytes have enhanced anaerobic glycolysis and decreased TCA cycle metabolism.

Mitochondria are central to energy metabolism and through the TCA cycle and oxidative phosphorylation they also produce reactive oxygen species (ROS).<sup>43</sup> We, thus, reasoned that, if the TCA cycle is altered, ROS levels in mutant astrocytes might also be impaired. Indeed, we found by MitoSOX staining that both R270X and R133C mutant astrocytes had significantly higher ROS levels compared with WT astrocytes (Figures 3E and S3L), indicating both oxidative stress and mitochondrial dysfunction.

One of the astrocyte's most important functions is removing the excitatory neurotransmitter glutamate from the synaptic cleft during neuronal activity<sup>34</sup> by uptaking and converting it to glutamine (Figure 3C right). Intracellular glutamate also plays roles in linking carbohydrate and amino acid metabolism via the TCA cycle, specifically via its conversion to  $\alpha$ -ketoglutarate (Figure 3C right). Glutamate uptake is mainly achieved by the two astrocyte-specific transporters, EAAT1 and EAAT2,<sup>44</sup> and the *SLC1A3* gene encoding EAAT1, was expressed in astrocytes in monoculture, but was down-regulated in mutant astrocytes (Figures 2E and S2F). We, therefore, analyzed the ability of mutant astrocytes to uptake glutamate. Both R270X or R133C astrocytes exhibited a significantly decreased capacity (65% and 25% decreases, respectively) to uptake glutamate (Figures 3F and S3M). Importantly, the extent to which these mutations decreased glutamate uptake correlated

directly with the extent to which the *SLC1A3* expression was down-regulated in the R270X-(4.4-fold) and R133C-(1.5-fold) mutant astrocytes (Figures 2E and S2F).

The impaired energy metabolism, redox balance, and neurotransmitter homeostasis suggest dysfunctional mitochondria in mutant astrocytes. Indeed, an analysis of mitochondrial respiration by Seahorse assay revealed dramatic reduction (approximately 50%) in their basal and maximal oxygen consumption in mutant astrocytes (Figures 3G and 3H). Furthermore, while analysis of mitochondrial mass by MitoTracker Green showed no difference between mutant and WT astrocytes (Figure S4A), an analysis of the mitochondrial morphology by MitoTracker Red revealed abnormal morphology in mutant astrocytes (Figures 3I and S4B). Specifically, while the mitochondria of most WT astrocytes had tubular and network-like structures, the mitochondria of most mutant astrocytes exhibited a rounded or fragmented appearance (Figures 3I, 3J, and S4B). Taken together, these data strongly suggest that the mitochondria in mutant human astrocytes are dysfunctional and likely mediate the alterations in bioenergetics, neurotransmitter homeostasis, and redox balance.

#### **RTT-causing *MECP2* mutations compromise both the neuron-dependent astrocyte stellate morphology and the astrocyte-dependent neuronal structural plasticity**

The interactions between neurons and astrocytes are bidirectional whereby astrocytes depend on neurons<sup>15,16</sup> and neurons depend on astrocytes for their structural and functional maturation.<sup>45</sup> Several GO terms suggest aberrant expression of genes involved in structural integrity in mutant astrocytes (Figure 2B). We therefore asked how *MECP2* mutations in human astrocytes and/or neurons affect the morphology of astrocytes and neurons. We first exploited a neuron-astrocyte co-culture system to examine the cell- and non-cell-autonomous effects of the R270X and R133C mutations. To analyze the neuron-dependent morphological changes in astrocytes, we transfected the neuron-astrocyte co-cultures, composed of different combinations of WT and mutant neurons and astrocytes, with a GFAP-enhanced green fluorescent protein (EGFP) construct and performed Sholl analysis on single GFAP-EGFP<sup>+</sup>/GFAP<sup>+</sup> astrocytes. As expected, neurons were able to transform the polygon-like flat shape of the astrocytes into a stellate morphology (Figure 4A). When we co-cultured WT astrocytes with mutant neurons, however, their structural complexity was significantly decreased, and they had a relatively shorter total branch length and fewer primary branches compared with WT astrocytes co-cultured with WT neurons (Figures 4A–4C). Importantly, when we co-cultured mutant astrocytes with WT neurons, mutant astrocytes acquired a more complex morphology compared with mutant astrocytes co-cultured with mutant neurons, but not to the extent observed when WT astrocytes were co-cultured with WT neurons (Figures 4A–4C).

Human astrocytes can respond to signaling from mouse or rat neurons and preserve their mature cellular and molecular features, which are largely intrinsically programmed.<sup>14,46</sup> We, therefore, asked whether xenografting mutant astrocytes into a WT mouse brain could provide a better environmental signaling platform to rescue their aberrant morphology. We xenografted EGFP-labeled R270X mutant or WT APCs into the corpus callosum area of immune-deficient *Rag1* mouse brains at post-natal days 0–1 (Figure S5A). Twenty

Author Manuscript  
Author Manuscript  
Author Manuscript  
Author Manuscript

weeks after transplantation, the engrafted WT and mutant APCs integrated into the host cortex and maintained their astroglial lineage properties, as indicated by SOX9 and human GFAP expression (Figures S5B and S5C). Notably, both WT and mutant human APCs differentiated into astrocytes and acquired a more complex stellate morphology than in the co-culture platform (compare Figures S5C and 4A). Sholl analysis revealed, however, that the transplanted mutant human astrocytes still had a significantly reduced morphological complexity compared with WT human astrocytes (Figures S5D–S5F). These observations support our co-culture data and further emphasize that the intrinsic mechanisms designed to support the neuron-dependent structural features of mutant astrocytes are severely impaired, impeding full morphological rescue by the normal mouse brain environment.

Next, we asked how *MECP2* mutations affect astrocyte-dependent neuronal structural plasticity. We first examined neuronal dendritic morphology by transfecting the neuron-astrocyte co-cultures with a CaMKII-EGFP construct (Figure 4D). Sholl analysis of single CaMKII-EGFP<sup>+</sup>/MAP2<sup>+</sup> neurons showed that R270X mutant astrocytes co-cultured with WT neurons robustly and negatively impacted the structural complexity of the WT neurons (Figures 4D–4F). When we co-cultured WT astrocytes with mutant neurons, mutant neuron morphology substantially improved (compared with mutant neurons co-cultured with mutant astrocytes), but did not reach the level of complexity observed in WT neurons co-cultured with WT astrocytes (Figures 4D–4F). In fact, the cell- and non-cell-autonomous effects of *MECP2* mutations on neuronal morphology mirrored the effects of the mutations on astrocyte morphology (compare Figures 4E and 4F with 4B and 4C). Importantly, both the R270X and R133C mutations produced similar effects on neuron-dependent astrocyte morphology and astrocyte-dependent neuronal morphology (Figures S6A–S6D). However, the loss of astrocyte and neuronal structural complexity due to R133C mutation was not as severe as with the R270X mutation, consistent with the R133C being milder than R270X mutation in RTT patients.

We then analyzed whether *MECP2* mutations in human neurons and/or human astrocytes impact synapse formation. We cultured mutant and WT neurons alone or co-cultured them with either WT or mutant astrocytes and then analyzed the density of SYN1 puncta and SYN1 (pre-synaptic)/Homer1 (post-synaptic) co-localized puncta along neuronal (TUJ1) processes (Figure 4G). Consistent with prior studies,<sup>47</sup> we found that WT astrocytes enhanced synapse formation when co-cultured with WT neurons compared with WT neurons cultured alone (Figures 4G and 4H). While mutant astrocytes were also able to enhance synapse formation in WT neurons, they were less efficient than WT astrocytes (Figures 4G and 4H black bar graphs). Mutant neurons cultured alone had a significantly reduced synaptic density compared with WT neurons cultured alone. As with WT neurons, WT astrocytes also enhanced synapse formation in mutant neurons more efficiently than mutant astrocytes (Figures 4G and 4H gray bar graphs); however, the synaptic density observed when mutant neurons were co-cultured with WT astrocytes did not reach the level observed when WT neurons were co-cultured with WT astrocytes (Figures 4G and 4H), likely due to cell-intrinsic aberrations in mutant neurons.

Collectively, our data suggest that *MECP2* mutations in neurons and astrocytes similarly affect both neuron-dependent astrocyte morphology and astrocyte-dependent neuronal

structural plasticity, and, in both cases, a combination of cell- and non-cell-autonomous defects causes the impaired morphology.

### **Mutant astrocytes generated and matured to a postnatal-like stage in three-dimensional human cortical spheroids are structurally and metabolically compromised**

The human cortical spheroids (hCSs)<sup>48,49</sup> provide a unique platform to model dorsal forebrain development in general and astrocyte developmental maturation in particular. Similar to *in vivo* brain development, first neurons are generated from NPCs in the ventricular-like zone (VZ), followed by the generation of astrocytes. Importantly, astrocytes proliferate and then continue to mature over time to a post-natal-like stage.<sup>48,49</sup> As RTT has a post-natal onset, we generated RTT and WT hCSs from R270X mutant and WT ESCs (Figure 5A) and analyzed them at different time points. Interestingly, while the WT and RTT hCSs began growing at similar rates, the RTT hCSs showed obvious stagnation over time (Figure 5B), echoing the microcephaly observed in RTT patients and mouse models.<sup>50,51</sup> This phenomenon could be the result of a reduced process complexity in both neurons and astrocytes. To eliminate the possibility that higher cell death in the RTT hCSs contributes to their smaller size, we immunostained sectioned spheroids for cleaved Caspase-3, a marker for apoptosis, and found no difference in the fraction of Caspase-3-positive cells (approximately 2%) between WT and RTT spheroids (Figure S7A). Immunostaining of 43-day-old hCSs (early development) showed VZ-like structures organized around lumens and the beginnings of neuronal differentiation around the VZ regions in both RTT and WT hCSs (Figure S7B). At day 110, we observed cortical layer formation as inferred by expression of the deep layer neuronal marker CTIP2 in both WT and RTT hCSs (Figure S7C). An analysis of hCSs at days 110 and 240 showed that both neurons ( $TUJ1^+$ ) and astrocytes ( $GFAP^+$ ) are present in RTT and WT hCSs, and the number of astrocytes increased over time (Figures 5C and 5D). To assess whether *MECP2* mutations affect the fraction of astrocytes and/or neurons generated in the developing hCSs, we dissociated RTT and WT hCSs to single cells at day approximately 200 and immunostained for neuron (MAP2)- and astrocyte (GFAP)-specific markers. This analysis showed comparable ratios of neuron-to-astrocyte production in RTT and WT hCSs (approximately 80% neurons to approximately 18% astrocytes) (Figures 5E right, 5F middle). In addition, more than 90% of the MAP2 $^+$  neurons were VGluT1 $^+$  excitatory neurons (Figure 5F right). As reported,<sup>21,52,53</sup> the nuclear size of mutant neurons was significantly smaller than that of the WT neurons; however, there was no difference in the nuclear size between WT and mutant astrocytes (Figures 5E and 5F left).

We then examined astrocyte and neuron morphology by transfecting the dissociated cultures with either GFAP-EGFP or CaMKII-EGFP (Figures 5G and 5J). Notably, Sholl analysis of single GFAP-EGFP $^+$ /GFAP $^+$  astrocytes revealed that WT astrocytes acquired complex morphology with highly ramified processes, but the morphology of mutant astrocytes was severely compromised (Figures 5G–5I). Furthermore, Sholl analysis of single CaMKII-EGFP $^+$ /MAP2 $^+$  neurons showed significantly reduced dendritic complexity in mutant neurons (Figures 5J–5L). Consistent with our co-culture data (Figures 4G and 4H), we found a dramatic decrease in SYN1 and co-localized SYN1/Homer1 synaptic density, and significant decrease in SYN1 puncta size in RTT hCSs (Figures 5M–5O).

Astrocytes generated in long-term hCSs continue to mature to a post-natal-like stage—at least in terms of gene expression landscape and structural complexity—after day 250.<sup>48</sup> We, therefore, maintained the RTT and WT hCSs for approximately 500 days in culture and isolated the astrocytes via immunopanning using anti-HepaCAM antibodies (Figure 6A). Immunostaining of the HepaCAM-positive and -negative cultures showed highly enriched GFAP<sup>+</sup> astrocytes and TUJ1<sup>+</sup> neurons, respectively (Figure 6B). Furthermore, the GFAP<sup>+</sup> astrocytes retained the complex morphology with ramified processes and expressed SOX9 (Figure 6C). Sholl analysis of single immunopanned astrocytes transfected with GFAP-EGFP revealed that the WT astrocytes were by far more structurally complex than those in younger hCSs, including a robust increase in total process length, the number of primary branches, and maximum intersections (compare Figures 5G–5I with 6C–6E). Importantly, the immunopanned mutant astrocytes also showed significant increase in their structural complexity compared with those in younger spheroids. However, they remained structurally compromised in all the above parameters compared with their WT counterparts (Figures 6C–6E).

We then analyzed the astrocyte morphology in the postmortem brains of two female RTT patients with R255X mutation and those of two age- and postmortem interval-matched control females. We immunostained sections of the temporal lobes for GFAP and searched for single astrocytes with complex ramified processes. While we were able to capture many in normal females, astrocytes of the female RTT patients showed a dramatic reduction in their structural complexity (Figure S8). These data strongly support the aberrant morphology of *MECP2*-mutant human astrocytes observed in our *in vitro* models.

Finally, we examined the extracellular metabolic profile of the immunopanned astrocytes derived from RTT and WT hCSs at approximately day 500. Mutant ACM showed significantly higher lactate and lower pyruvate compared with WT ACM (Figures 6F and 6G), as did the mutant astrocytes in monoculture (Figures 3A and S3C). We found that neurons secreted much less lactate than astrocytes (Figure 6F), as reported.<sup>54</sup> Importantly, unlike astrocytes, there was no significant difference in the secreted lactate between mutant and WT neuron-conditioned media (Figure 6F). The more mature mutant astrocytes also exhibited a decreased capacity to uptake glutamate (Figure 6H). Finally, the mitochondrial ROS level in the immunopanned astrocytes was significantly elevated in mutant astrocytes (Figure 6I). In fact, the ROS level was much higher in the more mature postnatal-like mutant astrocytes than in the mutant astrocytes in monoculture (compare Figures 6I–3E). Taken together, these data suggest that mutant astrocytes, even when they reach higher maturation stages in a brain-like environment (hCSs), retain the same impaired energy metabolism, glutamate homeostasis, and redox balance that observed in less mature astrocytes grown in monoculture.

### **Mutant astrocytes can receive and respond to both mutant and WT neuronal signaling and induce neuron-dependent gene expression**

During maturation, astrocytes respond to neuronal signaling and up-regulate the expression of a specific set of genes, termed neuron-induced genes.<sup>16,55</sup> In fact, many of the mature astrocyte-enriched genes are neuron-induced genes. We, therefore, investigated whether

*MECP2* mutations in astrocytes and/or neurons influence the neuron-induced expression of these astrocyte genes. To this end, we cultured the R270X-mutant and WT astrocytes either alone or co-cultured them with EGFP<sup>+</sup> R270X-mutant or WT neurons and then isolated the astrocytes (EGFP negative) by FACS (Figure 7A) to examine the expression of neuron-induced astrocyte genes. We selected genes based on their involvement in astrocyte key functions (Figure S9 legend) and their expression levels in mutant compared with WT astrocytes in monoculture, based on our RNA-seq analysis: (1) similar to WT astrocytes, (2) up-regulated, and (3) down-regulated (Figure 7B). Surprisingly, neuron-induced genes, expressed at similar levels in mutant and WT astrocytes in monoculture were all efficiently up-regulated to comparable levels in mutant and WT astrocytes regardless of whether they were co-cultured with mutant or WT neurons (Figure 7B). Neuron-induced genes, expressed at higher or lower levels in the mutant astrocytes when cultured alone, were also efficiently induced in mutant and WT astrocytes by both mutant and WT neurons. However, even after induction, their expression remained aberrant in the same way as in mutant astrocytes in monoculture (Figure 7B). Importantly, we observed a similar trend when we performed these analyses with the R133C-mutant astrocytes and/or neurons (Figure S6E).

We also took advantage of the hCS platform to analyze the expression of selected neuron-induced astrocyte genes immediately after immunopanning of astrocytes from RTT and WT hCSs at approximately day 500. Notably, mature neuron-induced astrocyte genes expressed at very low but similar levels in mutant and WT astrocytes in monoculture and co-culture were up-regulated to high and similar levels in the more mature hCS-derived mutant and WT astrocytes (Figure S9A). Other genes expressed at similar levels in mutant and WT astrocyte in monoculture and up-regulated to similar levels in WT and mutant astrocytes in co-culture were up-regulated to even higher—but still similar—levels in the hCS-derived mutant and WT astrocytes (Figure S9B). Importantly, genes dysregulated in mutant astrocyte in monoculture and similarly dysregulated after induction by neurons in co-culture, remained aberrantly expressed in the hCS-derived mutant astrocytes, even though their expression was induced to higher levels in hCSs (Figure S9C).

Together, these findings unequivocally suggest that mutant and WT astrocytes can respond to both mutant and WT neuronal signaling and elicit neuron-induced gene expression with similar efficiency, but that neurons are unable to correct the astrocyte-intrinsic gene expression defects caused by *MECP2* mutations.

## DISCUSSION

In this study, we provide evidence that RTT-causing *MECP2* mutations critically impact the intrinsic properties of human astrocytes and their ability to interact with neurons in a way that supports their mutual structural and functional maturation.

Our transcriptome analysis showed that *MECP2* mutations exert widespread cell-autonomous effects on astrocyte gene expression, including expression of mature astrocyte-enriched genes, causing more gene up-regulation than down-regulation and thereby supporting the MeCP2 role as a transcriptional repressor in human astrocytes. Astrocyte maturation strongly depends on interactions with neighboring neurons, which induce the

Author Manuscript  
Author Manuscript  
Author Manuscript  
Author Manuscript

expression of many mature astrocyte genes. Notably, we showed that the specific aberrations in gene expression in mature mutant astrocytes likely stem from the astrocyte-intrinsic defects in gene expression rather than from aberrations in neuronal signaling necessary for their induction and represent enduring changes rather than developmental acceleration or delay in maturation.

Astrocytes have a key role in regulating overall brain bioenergetics. We showed that mutant human astrocytes exhibited impaired energy metabolism, as evidenced by decreased TCA cycle metabolites and impaired metabolic pathways coupled to TCA cycle, decreased cellular ATP levels, and increased LPC and lactate production and secretion. The up-regulation of glucose transporter genes and genes that encode glycolytic enzymes, and the enrichment of up-regulated genes involved in hypoxia and the PI3K-AKT pathways, further indicate anaerobic conditions and enhanced glycolysis<sup>56</sup> in mutant astrocytes. Of note, elevated lactate in blood and cerebrospinal fluid has been found in RTT patients.<sup>57–59</sup> Lactate—the end product of anaerobic glycolysis<sup>39,40</sup>—is an energy substrate mainly produced by astrocytes and shuttled to neurons in response to synaptic activity, a mechanism known as the astrocyte-to-neuron L-lactate shuttle.<sup>60,61</sup> Recent studies have also shown that lactate acts as a signaling molecule that stimulates neuronal excitability.<sup>40,61</sup> It is, thus, possible that the elevated lactate found in RTT patients is due to its higher production and secretion by mutant astrocytes, affecting both energy metabolism and neuronal excitability.

Another key role of astrocytes is regulating glutamate homeostasis. Glutamate serves as a major excitatory neurotransmitter in the brain and as a cellular metabolite important for linking carbohydrate and amino acid metabolism via TCA cycle.<sup>62</sup> During neuronal excitation, astrocytes uptake glutamate from the extracellular space via glutamate transporters<sup>33</sup> and convert it to nonexcitatory glutamine. This function is critical for maintaining an excitatory/inhibitory balance as elevated levels of glutamate at the synaptic cleft can lead to excitotoxicity.<sup>63</sup> In our study, mutant astrocytes failed to properly uptake glutamate, even when they matured to a post-natal-like stage and when the expression of the two glutamate transporter genes, *SLC1A3* and *SLC1A2*, was induced by neurons. This is likely due to the cell-autonomous decreased expression of the glutamate transporter gene, *SLC1A3*, and the reduced ATP level in mutant astrocytes, as this process is energy dependent.<sup>64,65</sup> The reduced ability of mutant astrocytes to uptake glutamate could explain, at least in part, the excitatory/inhibitory imbalance that leads to seizures in RTT patients.<sup>66–68</sup>

The above findings collectively converge on mitochondria—the primary energy-producing organelles—that play a central role, particularly in astrocytes, in the regulation of the overall brain bioenergetics, neurotransmitter homeostasis, and redox balance.<sup>34</sup> Our data indeed revealed robust changes in mitochondrial structure and function and suggest that mitochondrial dysfunction likely lies at the core of the impaired energy metabolism in mutant human astrocytes. In our study, elevated mitochondrial ROS levels increased as mutant astrocytes matured. Such redox imbalance could result from excessive ROS production due to the altered mitochondrial structure and/or uncoupling of mitochondrial respiration complexes.<sup>69</sup> Interestingly, we observed higher LPC—known to disrupt mitochondrial integrity and induce ROS production<sup>42</sup>—in mutant astrocytes. While elevated

Author Manuscript  
Author Manuscript  
Author Manuscript  
Author Manuscript

ROS levels could also stem from reduced antioxidants, expression of genes that encode antioxidant enzymes were not altered. Together, our findings strongly suggest that elevated ROS levels in mutant astrocytes are due to higher ROS production rather than inefficient ROS scavenging. Excessive mitochondrial ROS production can lead to oxidative damage and induce cellular senescence.<sup>43</sup> Indeed, elevated oxidative stress, oxidative damage, and cellular senescence have been found in RTT patients and RTT mouse models.<sup>70–73</sup> Mitochondrial dysfunction in the RTT brain has been suggested by several studies.<sup>74,75</sup> In addition, astrocytes of RTT mouse models display mitochondrial alterations and redox imbalance.<sup>35,36</sup> Because mitochondrial metabolism in astrocytes regulates overall brain bioenergetics, it is conceivable that impaired mitochondrial metabolism in mutant human astrocytes, as we show here, plays an important role in the brain pathology of RTT patients.

Collectively, our data indicate that *MECP2* mutations lead to cell-intrinsic changes in human astrocytes that affect their overall homeostasis, and this may impact astrocyte morphology as well. Neuron-astrocyte signaling is fundamental for inducing complex stellate morphology in astrocytes during maturation. This morphology enables astrocytes to carry out their diverse interactions with other glia, neurons, and capillary endothelial cells in the brain.<sup>18,34</sup> Thus, significantly compromised structural complexity of mutant human astrocytes likely has severe consequences on overall brain homeostasis. The impaired morphology of human astrocytes is also supported by our previous observations in mouse models where *MeCP2* loss *in vivo* negatively impacted both neuronal and astrocyte structural complexity.<sup>76</sup> It has been also shown by GFAP immunostaining that astrocytes in an RTT mouse model have fewer and poorly branched ramifications.<sup>35</sup> In addition, some of the alterations in transcriptomic and proteomic profiles, which have been identified in the brains of symptomatic RTT mice, correlate with aberrations in astrocyte morphology.<sup>77</sup> Interestingly, while we observed a marked decrease in the complexity of mutant astrocyte morphology, there was no change in the expression of GFAP, the main intermediate filament in astrocytes that provides structural support for primary branches.<sup>78</sup> It is possible that alterations in the expression of other cytoskeletal and extracellular matrix proteins involved in astrocyte stellate morphology contribute to the abnormal astrocyte morphology. Importantly, although WT neurons were able to alleviate the extensive loss of stellate morphology in mutant astrocytes, *in vitro* and *in vivo*, the severe cell-autonomous defects in mutant astrocytes likely prohibited the neurons from accomplishing a complete non-cell-autonomous rescue. Notably, our analysis of astrocyte morphology in the brains of postmortem female RTT patients revealed that, although approximately 50% of astrocytes express normal *MeCP2*, due to female mosaicism of X chromosome inactivation, all astrocytes showed severely stunted morphology. In agreement with our *in vitro* study herein, these findings suggest that, in addition to the cell-intrinsic aberrations in mutant human astrocytes that negatively affect their stellate morphology, there are also significant negative non-cell-autonomous effects of the RTT brain environment on astrocyte morphology. Such effects could be due to a lack of proper physical interactions between neurons and astrocytes in the mosaic female RTT brain and/or aberrant secretion of proteins and metabolites by mutant neurons and glia.

Finally, we sought to examine how all these molecular and structural consequences of *MECP2* mutations in human astrocytes affect neurons, as astrocytes play a central role in supporting their structural plasticity, including dendritic arborization, synapse formation,

Author Manuscript  
Author Manuscript  
Author Manuscript  
Author Manuscript

and synapse elimination.<sup>12,79</sup> Mutant human astrocytes insufficiently supported the dendritic arborization of human neurons, which is consistent with our own studies in mouse models<sup>5,7</sup> and other studies using the mouse-human co-culture.<sup>9</sup> We also showed that synapse formation was severely impaired in mutant neurons due to both cell-autonomous defects and non-cell-autonomous effects of neighboring mutant astrocytes. Notably, in contrast with our previous findings in RTT mouse models, in which the WT mouse astrocytes were able to fully rescue the aberrant structural plasticity of mutant neurons,<sup>5,7</sup> the WT human astrocytes only partially alleviated dendritic arborization and synapse formation defects in mutant human neurons. This suggests that *MECP2* mutations have more severe consequences in neurons and astrocytes in the human brain than the rodent brain and may explain, at least in part, why the RTT patient phenotypes are more severe than mouse model phenotypes. Such differences between humans and rodents further imply that human RTT models are critical for elucidating the molecular and cellular mechanisms of RTT and developing therapeutic strategies.

We conclude that the different RTT-causing *MECP2* mutations lead to significant molecular and cellular impairments in human astrocytes that disrupt not only their intrinsic homeostasis, but also their interactions with neurons, ultimately reflecting on neuronal function. Notably, while the two RTT-causing mutations we examined generally caused similar aberrations, the severity of the cellular and molecular phenotypes correlated with the severity of the clinical phenotypes caused by the different mutations. We thus argue that comparing different mutations, especially at the molecular level, is critically important in deciphering the root causes of RTT pathology, identifying biomarkers, and designing therapeutic strategies against this devastating neurodevelopmental disorder.

### Limitations of the study

Our data suggest that *MECP2* mutations critically impair human astrocyte properties and that these changes likely have direct consequences for neuronal function. However, we have not determined which specific changes in mutant astrocytes mediate the specific aberrations in neurons. Further studies are needed to address this question.

The impaired astrocyte morphology we observed in post-mortem female RTT brains validates our *in vitro* human-based models of RTT. However, we need to recognize that *in vitro* models lack the full complexity of the brain, such as vascularization and the presence of other cell types. Regardless, these emerging human models combined with mouse models and studies of postmortem brains when available are invaluable in advancing our understanding of neurodevelopmental disorders not fully replicated in animal models, such as RTT, and accelerating the development of better therapies.

Although RTT almost exclusively occur in females, we chose to use male hPSCs to avoid potential confounders stemming from the unstable X-inactivation that often happens during the culturing of female hPSCs. Our data indicate that RTT-causing mutations are not sex biased with respect to astrocyte morphology; we identified similar aberrations in astrocyte morphology in the post-mortem brains of female RTT patients. However, further studies with female hPSCs are needed to confirm the data obtained with male hPSCs.

## STAR★METHODS

### RESOURCE AVAILABILITY

**Lead contact**—Further information and requests for resources and reagents should be directed to and will be fulfilled by the lead contact, Dr. Nurit Ballas (nurit.ballas@stonybrook.edu).

**Materials availability**—All unique/stable reagents and biological materials generated in this study are available from the lead contact upon request, with a completed Material Transfer Agreement.

#### Data and code availability

- RNA sequencing data have been deposited at NCBI GEO and are publicly available. The accession number is listed in the Key resources table.
- This paper does not report original code.
- Any additional information required to reanalyze the data reported in this paper is available from the lead contact upon request.

### EXPERIMENTAL MODEL AND SUBJECT DETAILS

**Human embryonic stem cell lines**—All human embryonic stem cell (hESC) studies were approved by the Embryonic Stem Cell Research Oversight Committee (ESCRO) at Stony Brook University. The male hESC line (H1) was obtained from WiCell Research Institute. The derivative H1 clones from genome editing were obtained as described.<sup>23</sup> Cells were characterized and maintained as detailed below.

**Animals**—All animal studies were approved by the Institutional Animal Care and Use Committee at Stony Brook University. Homozygous female and male immune-deficient Rag1<sup>-/-</sup> (B6.129S7-Rag1tm1Mom/J; Jackson Laboratory Cat#002216) mice were bred and housed under maximum isolation conditions. Male Rag1<sup>-/-</sup> neonates were used for transplantation at postnatal day 0–1.

**Postmortem human temporal lobe specimens**—All postmortem brain studies were approved by the Institutional Review Board at Stony Brook University. Age- and PMI-matched postmortem human temporal lobe specimens from control female donors and female RTT patients with R255X mutation were acquired from NIH NeuroBioBank/University of Maryland brain bank. The median age of the control females and female RTT patients was 19. All available deidentified patient data are listed in Table S5.

### METHOD DETAILS

**CRISPR/Cas9-based genome editing and characterization of hESC cultures**—The RTT-causing mutations in *MECP2*, R270X and R133C, were introduced into a male H1 human embryonic stem cell (hESC) line using CRISPR/Cas9-based genome editing.<sup>23</sup> In brief, sgRNA was selected using a CRISPR Design Tool and the corresponding coding sequence was cloned into pSpCas9(BB)-2A-Puro (PX459) construct. Single stranded oligo

Author Manuscript  
Author Manuscript  
Author Manuscript  
Author Manuscript

donors were used to introduce the desired point-mutation that targets the MBD domain (R133C) or the TRD domain (R270X) in *MECP2*. Successfully targeted human clones were identified according to their target sequences and expanded for downstream use. H1 hESCs and all derivative clones from genome editing were maintained on Matrigel (BD Biosciences) coated plates with mTeSR1 or mTeSR Plus medium (STEMCELL Technologies). Cells were passaged with Gentle Cell Dissociation Reagent (STEMCELL Technologies) and kept in a humidified incubator at 37°C, 5% CO<sub>2</sub>.

Karyotyping, by standard G-banding technique, was performed by Cell Line Genetics (Madison, WI). Genotyping of hESC lines was performed by extracting genomic DNA, using a QIAamp DNA kit (Qiagen) and sequencing.<sup>80</sup> The primers used for amplifying human *MECP2* sequences in mutant and the isogenic wild-type counterpart lines are listed in Key resources table. The gel purified PCR products were sequenced directly. Pluripotency was assessed by immunostaining for the pluripotency markers OCT4, SOX2 and NANOG.

**Differentiation of hESCs into cortical astrocytes and neurons in monolayer—**  
On day 0 of differentiation, any pre-differentiated cells in the hESC cultures were removed by scrapping. hESCs were dissociated into single cells with Gentle Dissociation Reagent, and 1.5 × 10<sup>6</sup> cells were plated into one well of AggreWell plate (STEMCELL Technologies #34811) in embryoid body (EB) medium containing DMEM-F12 (Gibco #11330032), 20% KnockOut Serum Replacement (Gibco #10828010), 1% NEAA (Gibco #1140050), 0.5% GlutaMAX (Gibco #35050), 100 μM β-mercaptoethanol (Sigma-Aldrich #M3148), 10 μM SB431542 (Abcam #AB120163), 1 μM Dorsomorphin (Tocris), and was supplemented with the ROCK inhibitor Thiazovivin (0.5 μM). EB medium was gradually replaced by discarding half of the medium every day for 6 days and adding N2B27 medium containing DMEM-F12, 1% N2 (Gibco 17502048), 2% B27 supplement without vitamin A (Gibco #12587010), 0.5% Glutamax, 1% Penicillin/Streptomycin and supplemented with 10 μM SB431542 (SB), 1 μM Dorsomorphin (DM). On Day 7, EBs were released from the AggreWell Plate, transferred to an ultra-low attachment plate and cultured in suspension in N2B27 medium supplemented with 20 ng/mL bFGF (Peprotech 100–18B), 3 μM CHIR 99021 (Axon Medchem), 0.5 μM PMA (Alexis) and 150 μM ascorbic acid (Sigma-Aldrich) with medium change every other day, until neural tube-like structures appeared.<sup>81</sup> At day 12, neural tube-like structures were manually selected and plated onto a Matrigel-coated plate in N2B27 medium with 20 ng/mL bFGF, and media was replenished every other day. On day 19, neural rosette-like structures were isolated from surrounding cells with Neural Rosette Selection Reagent (STEMCELL Technologies #05832) and expanded as human neural progenitor cells (NPCs) on a Matrigel-coated plate in N2B27 medium supplemented with bFGF (40 ng/mL), EGF (40 ng/mL, R&D systems #236-EG-200) and hLIF (1.5 ng/mL, Peprotech 300–05). NPCs were passaged with Accutase (Gibco #A1110501) when they reached 70%–80% confluence.

For astrocyte differentiation, NPCs were differentiated into astrocyte progenitor cells (APCs) by culturing on Matrigel-coated plates and passaging in N2B27 medium supplemented with BMP4 (10 ng/mL, Peprotech) and bFGF (20 ng/mL) for 21–25 days, after which they were FACS-sorted for CD44 and propagated. The CD44-positive APCs were then differentiated to astrocytes by culturing in astrocyte maturation medium containing N2B27

medium supplemented with CNTF (10 ng/mL, Peprotech), LIF (10 ng/mL, Peprotech) and FGF-1 (50 ng/mL, Peprotech) for up to 48 days.<sup>29</sup>

For neuronal differentiation, NPCs were plated on poly-L-ornithine (0.1 mg/mL, Sigma-Aldrich #P3655) and laminin (10 µg/mL, Corning #354232) pre-coated 12mm glass coverslips (Ted Pella #26020) or cell culture plates, at a density of 15,000 cells/cm<sup>2</sup> in N2B27 medium. To differentiate the NPCs into neurons, half of the medium was changed every other day with neuronal differentiation medium containing BrainPhys<sup>TM</sup> Neuronal Medium (STEMCELL Technologies), supplemented with 1% N2, 2% B27, BDNF (brain-derived neurotrophic factor), 20 ng/mL, Peprotech 450–02), GDNF (glial cell line-derived neurotrophic factor), 20 ng/mL, Peprotech 450–10), ascorbic acid (200 nM, Sigma-Aldrich A0278), and dibutyryl-cAMP (1mM, Sigma-Aldrich D0627).<sup>82</sup>

**Fluorescence-activated cell sorting (FACS)**—To enrich for CD44-positive APCs, APC cultures generated from NSCs were dissociated with Accutase and cell suspension was incubated with FITC-conjugated CD44 antibody (BD Biosciences 560977) for 20 min on ice in the dark and then washed twice with sorting medium (N2B27 medium, 0.5% BSA, 50 mM EDTA, DNase (100 mg/mL). FITC-positive cells were collected using a FACSaria III cell sorter (BD Biosciences) and cultured for APCs.

**Immunocytochemistry**—Cells cultured on coverslips were fixed in PBS-4% paraformaldehyde (PFA) at room temperature for 15 min and then washed in PBS three times. Fixed cells were permeabilized with PBS-0.1% Triton (PBST) for 15 min, incubated in blocking buffer (PBST, 2% BSA, 5% Donkey or Goat serum) for 1h at room temperature and then incubated at 4°C overnight with primary antibodies (see Key resources table) diluted in blocking buffer. On the second day, primary antibodies were washed off with PBST and the coverslips were incubated for 1 h at room temperature with appropriate secondary antibodies (see Key resources table). Secondary antibodies were washed off with PBST and coverslips were mounted using Vectashield antifade mounting medium containing DAPI (Vector Labs) for nuclei labeling. Images were collected on a Leica (TCS-SP5) or Zeiss (LSM 700) laser scanning confocal microscope. Images were captured and analyzed blind to genotype.

**Quantification of fluorescence intensity**—Cells were imaged with Leica confocal microscope with three to five random fields imaged per group in each biological replicate. To measure fluorescence intensity, we used ImageJ (NIH) software as follows: The regions of specific markers were selected, and fluorescence intensity was measured by using ‘area integrated intensity’ in ‘measure’ tool. Background fluorescence intensity in region without cells was measured and subtracted. The relative fluorescence intensity was compared to the average intensity of wild-type cells in each group. Images were taken and quantified blind to genotype.

**RNA isolation and quantitative real-time RT-PCR**—Total RNA was extracted using the miRNeasy Mini Kit (Qiagen) or the TRIzol (Invitrogen) method. For reverse transcription, AMV-RT (New England BioLabs) was used. The quantitative real-time PCR was performed by ABI StepOnePlus real-time PCR system using SYBR green PCR master

mix (Applied Biosystems). Data was analyzed using StepOne software and Prism. Primers used for qPCR analyses are listed in Table S4.

**Total RNA library preparation and RNA-Sequencing analysis**—Total RNA was extracted using the miRNeasy Mini Kit (Qiagen) following the manufacturer's protocol. RNA integrity was assessed by Bioanalyzer. All RNA samples had RNA Integrity Number (RIN) of at least 8.4. The RNA samples were sequenced on an Illumina NovaSeq 6000 Sequencing System and yielded about 20–30 million pairs of 150 bp pair-end reads per sample. Raw reads were first trimmed for 10 bases at the 5' end to remove reads with biased nucleotide (ACGT) distribution. Trimmed reads were then aligned to the *Homo sapiens* genome (GRCh38p12, GENCODE, primary assembly), using STAR aligner<sup>83</sup> (version 2.6.0a). Differential gene expression (DEG) analyses on the read counts were performed using DESeq2<sup>84</sup> (v1.24.0) in R environment. Genes with sum of read counts across all samples under 10 were filtered out from analysis. Unless otherwise stated, a gene was considered significantly dysregulated if the adjusted p value was less than 5% and with a minimum average read counts of 10 in either genotype.

Expression heatmaps were generated using the pheatmap package in R environment. Genes with adjusted p value <5% and well-expressed, with a minimum average read counts of 50 in mutant and/or WT astrocytes, were used for fetal and mature astrocyte enriched gene heatmap. The heatmaps are normalized across each gene (row) and the color legend shows Z score. Specifically, this was carried out in two steps: 1) the mean expression for the gene (the specific row) was subtracted out from each expression, 2) the mean-centered expression was divided by the standard deviation for the gene. Gene Set Enrichment Analysis (GSEA) software<sup>85</sup> was used to assess the enrichment of the significantly dysregulated genes in the gene sets enriched in fetal astrocytes and mature astrocytes.<sup>11</sup>

**Gene ontology analysis**—Gene ontology (GO) enrichment analysis was performed using the DAVID v6.8 bioinformatics resource (<http://david.abcc.ncifcrf.gov/>).<sup>86,87</sup> Genes with adjusted p value less than 0.05 and normalized read counts >50 in mutant and/or WT were used for the GO enrichment analysis. The significantly enriched GO terms were selected based on Benjamini corrected p-values <0.05 cut-off, and biological relevance to the study.

**Generation of astrocyte conditioned media and intracellular metabolite extraction for <sup>1</sup>H NMR and mass spectroscopy**—For <sup>1</sup>H NMR and untargeted mass spectrometry of extracellular metabolites, astrocyte conditioned media (ACM) was collected at day 48 of differentiation of APCs into astrocytes (3 days after changing the medium at day 45). The collected ACM was centrifuged at 2000g for 5 min and the supernatant was aliquoted and kept frozen at -80°C. For <sup>1</sup>H NMR and targeted mass spectrometry of intracellular metabolites, astrocytes were washed three times with PBS, dissociated with Accutase for 5 min at 37°C, and washed 3 times with PBS with centrifugation. After the last centrifugation, pellets were resuspended in PBS and counted. Cells (1.6 million) were centrifuged at 3000g for 10 min at 4°C and frozen pellets were kept at -80°C.

**NMR spectroscopy**—For extracellular metabolite analysis, 450 µL ACM was mixed with 50 µL Deuterium oxide ( $D_2O$ , 99.9% D) containing 5 mM DSS (4,4-dimethyl-4-silapentane-1-sulfonic acid) (Cambridge Isotope Laboratories, Inc) as an internal standard ( $\delta = 0.00$  ppm). 1D  $^1H$ -NMR spectra were acquired on a Bruker 850 MHz NMR spectrometer with cryoprobe. The water peak was suppressed by presaturation, using the 1D zgpr pulse sequence from the Bruker pulse sequence library, applying a low power suppression continued wave irradiation before the first 90 pulse on channel 1. The numbers of scans and dummy scans were 16 and 4, respectively.

For intracellular metabolite analysis, the frozen cell pellets were thawed on ice, resuspended in 450 µL PBS, and mixed with 50 µL Deuterium oxide ( $D_2O$ , 99.9% D) containing 5 mM TSP (Trimethylsilylpropanoic acid,  $\delta = -0.01581$  ppm) as an internal standard. 1D and 2D  $^1H$ -NMR spectra were acquired on a Bruker 800 MHz AVANCE III NMR spectrometer equipped with cryoprobe. The 1D spectra were acquired with the Bruker standard pulse sequence NOSEYPR1D with water presaturation. Acquisition mode was DQD, number of time domain points = 32768, spectral width = 20.5583 ppm. The experiments were recorded without sample spinning. The power level and the duration of the presaturation were PLdb9 = 23 dB and d1 = 2s, respectively. The mixing NOESY time was 100 ms. The on-resonance to the solvent resonance o1 was finely adjusted in gs mode by minimizing the FID signal intensity. The obtained spectra were pre-processed with chemical shift calibration, phase correction, and baseline correction, and converted to TXT file for the multivariate analysis. Estimated metabolite concentration was obtained using Chenomx, Inc. software. The 2D total homonuclear correlation spectra was obtained via Hartman-Hahn transfer using dipsi2esgpph sequence using 3–9–19 watergate (DIPSI-2). The spectral width: 13.95. Size of FID is 4096 (F2) X2048 (F1). The power level of the pulses: PLdb18 = -11.76dB. The 90-degree pulse: PLdb18 P27 = 10Sec. The mixing time: d9 = 60 ms. The duration pf the gradient p16 = 1 ms. The recovery delay after the gradient d16 = 200 us. GPZ1% = 1. Gpnam1 = SMSQ10.100. The number scan was 24 with dummy scans equal to 160.

For multivariate analysis, the obtained spectra were pre-processed with chemical shift calibration, phase correction, baseline correction and subjected to multivariate analysis including PCA (principal component analysis) for data summary and OPLS (Orthogonal partial least squares) for regression analysis by SIMCA P software.

**Non-targeted liquid chromatography with tandem mass spectrometry (LC-MS/MS)**—Samples were prepared by mixing 20 µL ACM with 60 µL of ice-cold methanol with internal standards (agomelatine for positive mode; lithocholic acid-d5 for negative mode). The resulting mixtures were vortexed and centrifuged at 15,000 g for 15 min. A 5 µL volume of the prepared samples was injected onto a system combining ultra-high performance liquid chromatography (UHPLC) coupled with Q Exactive Orbitrap mass spectrometer (Thermo Fisher Scientific) equipped with 100 mm × 2.1 mm column (Acquity 1.7 µm, BEH C-18, Waters) for analysis. The column temperature was maintained at 40°C. Flow rate was set to 0.3 mL per minute and the autosampler sample tray to 10°C. Mobile Phase A was water with 0.1% formic acid. Mobile Phase B was acetonitrile 0.1% formic acid. The chromatographic gradient was as follows: (1) 0–16 min: linear gradient from 2% to 98%

B; (2) 16.0–19 min: hold at 98% B; (3) 19.0–20.0 min: linear gradient from 98% to 2% B and hold at 2% B till 22.0 min. Q Exactive MS was operated in full scan with electrospray ionization in positive mode and negative modes. Ultra-highly pure nitrogen was applied as the sheath (45 arbitrary unit), auxiliary (10 arbitrary unit), sweep (1.0 arbitrary unit) and the collision gas. The capillary gas temperature was set at 275°C and the capillary voltage was set at 3.75 kV for positive mode and 2.75 kV for negative mode. MS data were acquired from 80 to 1200 Da with the resolution set to 140,000, and the maximum injection time at 100 msec in profile mode. The acquired data were processed by Compound Discoverer 3.0 software to generate a multivariate data matrix. The data was first normalized based on protein concentration of the sample and the internal standards. The normalized data matrices were subject to multivariate data analysis on SIMCA14 software (Umetrics, Kinnelon, NJ). Orthogonal projection to latent structures-discriminant analysis (OPLS-DA) was conducted on Pareto-scaled data for determining the primary metabolites contributing to group difference.

**Metabolite Identification and Confirmation:** Putative structures of lysophosphatidylcholine (LPC) and succinic acid were identified based on MS/MS fragments, exact mass, and predicted formula structure of metabolite obtained from Q Exactive MS. Their structures were confirmed by comparing their exact mass, MS/MS fragments, and retention times with those of the corresponding commercially available standards.

**Targeted mass spectrometry**—The intracellular metabolites were extracted from monocultured astrocytes and mouse liver pool was used as quality control.<sup>88–90</sup> The TCA metabolites and glycolysis intermediates were separated using Luna 3 μM NH<sub>2</sub> (100 A°) HPLC column, whereas mobile phase was A and B in 20 mM ammonium acetate in water (pH 9.9) and acetonitrile, respectively. The metabolites were separated through Agilent HPLC system, and the data acquired using 6490 triple quadrupole mass spectrometry (Agilent Technologies, Santa Clara, CA) via Multiple reaction monitoring (MRM) in negative ionization mode.<sup>90</sup> The acquired data were analyzed using Agilent Mass Hunter quantitation software and carefully reviewed for all peaks sample-by- sample. The peak areas were first normalized to a spiked internal standard L-Zeatin (ISTD), then normalized to the abundance in WT samples (log<sub>2</sub> scale). The altered metabolites were identified using Benjamin-Hochberg p values <0.25 false discovery rate (FDR).

**Glutamate uptake assay**—The Amplex Red Glutamic Acid/Glutamate Oxidase Assay Kit (Invitrogen) was used following manufacturer's instructions.<sup>29</sup> Astrocytes were plated at a concentration of 10,000 cells per well in 96 well plate and cultured for 2 days (for monocultured astrocytes) or 7 days (for hCS-derived astrocytes). Before the assay, cultures were equilibrated in HBSS buffer for 10 min. L-Glutamate (20 μM) solutions were prepared with HBSS and added to the cells. After 30 min, the glutamate concentration remaining in the media was measured. The decrease of glutamate in the media, or uptake of glutamate by cells, was measured as micromoles of glutamate per microgram of protein after being normalized to the total protein in each well. For normalization purpose, the protein content was determined by a BCA protein assay (Pierce).

**ATP assay**—ATP levels were determined using an ATP Bioluminescence Assay Kit (PerkinElmer).<sup>91</sup> In brief, astrocytes were harvested using the provided cell lysis solution and incubated on ice. The ATP levels in the cells were measured using a luminescence plate reader (Molecular Devices) and normalized to the total protein in each well.

**MitoSOX assay**—Mitochondrial ROS was determined using MitoSOX Red (Invitrogen). Cells were plated onto coverslips. Upon analysis, cells were incubated with complete cell culture medium containing 2.5  $\mu$ M MitoSOX for 20 min at 37°C in tissue culture incubator. Cells were then washed twice with PBS, fixed, incubated in blocking buffer (PBST, 2% BSA with 5% goat serum) for 1 h and incubated with rabbit anti-GFAP antibody at 4°C overnight, followed by incubation with Alexa Fluor 488 conjugated goat anti-rabbit for 1 h at room temperature. Fluorescence images for GFAP and MitoSOX were acquired with confocal microscope. Fluorescence intensity of MitoSOX was measured using ImageJ software (NIH). Each single astrocyte was identified by GFAP staining and thresholded to define the cell area as region of interest (ROI).<sup>91,92</sup> The MitoSOX fluorescence of each cell was then measured with the ROI Manager, and background fluorescence was subtracted. For each biological replicate, 5–10 field of images were taken and a total of 33–40 cells were analyzed for each genotype. Images were taken and quantified blind to genotype.

**Seahorse measurement of cellular respiration**—Seahorse measurement of cellular respiration was performed using a Seahorse extracellular flux analyzer and XF Mito Stress kit (Agilent) according to the manufacturer's protocol. In brief, 50,000 or 75,000 astrocytes were plated per well on a Matrigel coated XF 96-cell culture plate 3 days before the measurement and incubated in 37°C and 5% CO<sub>2</sub> in a humidified incubator. Cells were cultured in 8 wells per group as technical replicates. On the day of measurement, cells were washed with XF cell Mito stress test assay medium containing Seahorse XF DMEM media (phenol red free), 10 mM glucose, 1 mM Pyruvate and 2 mM L-Glutamine. Cells were incubated in the assay medium for 1 h prior to the measurement in a CO<sub>2</sub>-free incubator at 37°C. During the measurement assay, inhibitors were loaded into cells at final concentration of 1.0  $\mu$ M Oligomycin (Port A), 2  $\mu$ M FCCP (Port B) and 0.5  $\mu$ M Rotenone/antimycin A (Port C). Results of the measurement were subsequently analyzed using the Wave software (Agilent). Data was normalized by cell number as determined by Hoechst staining. OCR was presented as pmol/min per 100,000 cells.

**Mitochondrial morphology (MitoTracker red)**—For analysis of mitochondrial morphology, astrocytes were plated onto Matrigel coated coverslips and incubated in 400 nM MitoTracker CMX Red (M7512, Invitrogen) diluted in complete cell culture medium for 15 min at 37°C and 5% CO<sub>2</sub> in a humidified incubator. Cells were washed three times, fixed, counterstained with 1  $\mu$ g/mL Hoechst and imaged with confocal microscope (Leica) with an oil-immersed 63 $\times$  objective. Images were acquired blind to genotype. For analysis of mitochondrial morphology, cells were categorized as having tubular/network-like or circular/fragmented mitochondria if more than 70% of their mitochondria show the specific structure. Otherwise, they were categorized as having mixed structures.

**Mitochondrial mass (MitoTracker green)**—Astrocytes were plated at 25,000 per well on Matrigel coated dark-welled flat bottom 96-well plate (Sarstedt) two days before the assay. Cultured astrocytes were incubated with 250  $\mu$ M MitoTracker Green FM (MTG, Thermo Fisher M7514) and 1  $\mu$ g/mL Hoechst for 20 min in astrocyte culture media at 37°C and 5% CO<sub>2</sub> incubator. Cells were washed three times in culture media to remove extra MTG and Hoechst dyes. Whole well fluorescence for MTG and Hoechst intensity were measured with FilterMax plate reader (Molecular Devices), set to appropriate wavelengths. The intensity of MTG was normalized to cell number based on Hoechst intensity.

**Generation of lentivirus**—Lentivirus carrying UbiquitinC-EGFP was generated by co-transfected HEK293T cells with pFUGW plasmid, containing the EGFP gene under UbiquitinC promoter, and the packaging plasmids VSV-G and 8.9. Transfection was performed using Mirus 293T transfection reagent.<sup>93</sup> After 24 h from transfection, the medium was discarded and replaced with N2B27 medium for 2 days. The medium containing lentiviruses was collected, filtered through 0.45  $\mu$ M, aliquoted and frozen at -80°C.

**Neuron-astrocyte co-culture**—For astrocyte-neuron co-cultures, APCs were differentiated into astrocytes in astrocyte maturation medium for 27 days and replated onto Matrigel coated tissue culture plates or poly-L-ornithine/laminin coated coverslips at a density of 15,000 cells per cm<sup>2</sup>. NPCs were differentiated for 7 days in neuronal differentiation medium, dissociated with Accutase, and replated onto the astrocytes at a plating density of 15,000 cells per cm<sup>2</sup>. The neuron-astrocyte co-cultures were maintained on coverslips in N2B27 medium for 21 days for morphology analysis, and 10 weeks for synapse formation analysis with half medium changed every other day.

For astrocyte gene expression analysis in neuron-astrocyte co-cultures, NPCs were transduced with UbiquitinC-EGFP lentivirus (95% labeling efficiency), differentiated into EGFP + neurons using the differentiation method described above, and plated onto astrocytes cultured on Matrigel coated plates. The co-cultures were maintained in N2B27 medium for 21 days, with half medium changed every other day. On the day of collection, astrocytes cultured alone and neuron-astrocyte co-cultures were each dissociated with Accutase, resuspended in sorting media as single cell suspension, and sorted by fluorescence-activated cell sorting (FACS). EGFP negative (astrocytes) and positive (neurons) were separately collected into DPBS, centrifuged, and transferred immediately into TRIzol (Invitrogen) for RNA extraction.

**Morphological analysis of neurons and astrocytes in co-cultures**—To detect and trace single neurons, co-cultures on coverslips were transfected sparsely with CaMKII-EGFP using the calcium phosphate precipitation method with a CalPhos™ Mammalian Transfection Kit (Takara Inc.) on day 18 of co-culturing. To detect and trace single astrocytes, co-cultures were transfected with hGFAP-EGFP plasmid, using Mirus TransIT-2020 transfection reagent on day 18 of co-culturing. Cells were fixed with PBS-4% PFA, 3 days post-transfection, and immunostained with anti-EGFP and cell-type specific antibodies. GFP-positive cells were imaged with a Leica confocal laser-scanning (TCS-SP5) microscope. Confocal images were analyzed using ImageJ software including FIJI plug-in

Author Manuscript  
Author Manuscript  
Author Manuscript  
Author Manuscript

packages with a Sholl tracing package and simple neurite tracer.<sup>94</sup> To analyze synaptic density, cultured cells were fixed with PBS-4% PFA, immunostained with TUJ1 and pre-/post-synaptic antibodies (see details in immunocytochemistry and Key resources table). Images were acquired with a Leica confocal laser-scanning (TCS-SP5) with identical settings applied to all samples in an experiment. Synapsin 1 puncta (pre-synaptic) and co-localized Synapsin 1 and Homer1 (pos-synaptic) puncta along single TUJ1 processes were quantified from random images by ImageJ software (NIH).<sup>95</sup> Synapse puncta were identified by background subtraction and intensity threshold function in ImageJ and selected as the region of interest (ROI). ROIs were quantified with the ‘analyze particles’ plugin and neurite length were measured by ‘simple neurite tracer’ plugin. Synaptic density per 50 µm TUJ1 processes were calculated. All morphological analyses were performed blind to genotypes and conditions.

**Nuclear size measurement**—Dissociated hCSs (at day ~200) cultures were immunostained for cell type specific markers and counterstained with 1 µg/mL Hoechst. ImageJ (NIH) was used for the nuclear size measurement. All the images were taken with a 40× objective. In the software setting, with a line drawn around the Hoechst nuclear staining, the surface area size of the nuclei was automatically calculated. Student’s t test was used for statistical analysis.

**Transplantation**—For transplantation, CD44-sorted APCs were transduced with lentivirus carrying UbiquitinC-EGFP and cultured in N2B27 medium supplemented with BMP4 (10 ng/mL) and bFGF (20 ng/mL). More than 90% of cells were GFP positive. The EGFP labeled APCs were passaged with Accutase one day before transplantation and plated in ultra-low attachment plates at a density of 500,000 cells per ml to allow small cell clusters to form. Before transplantation, cells were spun down at 300g for 5 min and resuspended to 100,000 cells per µl in HBSS solution.

Rag1<sup>-/-</sup> neonates were transplanted between postnatal day 0 and 1. Half of the litter was transferred from the cage to a humidified warming chamber and the second half of the litter was kept with parents to avoid shock to the parents. The pup to be injected was anesthetized by hypothermia, wiped with an ethanol pad, and transplanted bilaterally with a total of 100,000 cells per hemisphere. The injection was performed directly through the skin and skull into caudal corpus callosum (AP –1.0, ML ± 1.0 mm, ventral 1.2 mm).<sup>96</sup> Following injections, the pup was cleaned with alcohol, placed in the warming chamber for 30 min for recovery and returned to the cage. After returning the first half of the litter, the injection was performed for the second half of the litter. Pups were weaned between 21 and 28 days and group housed.

**Immunohistochemistry of brain sections**—Chimeric mice were perfused transcardially with PBS-4% PFA at 19–20 weeks post transplantation. Brains were preserved in PBS-4% PFA overnight, washed with PBS, and sectioned with vibratome at 80 µm thickness. To immunostain the brain sections, sections were permeabilized with PBST for 25 min, blocked in 5% Goat 5% Donkey serum in PBST and immunostained with free-floating method.<sup>53</sup> The brain sections were incubated at 4°C overnight with primary antibodies (see Key resources table) in 1% Goat 1% Donkey serum in PBST. On the second day, primary

antibodies were washed off with PBST followed by incubation with secondary antibodies (See Key resources table). Nuclei were counterstained with 1 µg/mL Hoechst solution and sections were mounted onto glass slides using VECTASHIELD Antifade Mounting Medium (H-1000). Images were collected on a Leica confocal laser-scanning (TCS-SP5) microscope.

For morphological tracing of transplanted human astrocytes in the mouse brain, individual GFP-labeled astrocytes were randomly selected and traced using Neurolucida 360 (Micro Brightfield Inc) or z stack reconstructed confocal images with Sholl analysis plugin (ImageJ). Data were extracted for Sholl analysis and primary branches and total length for each cell was measured.<sup>53</sup> Imaging and morphological analyses were performed blind to genotype.

**Generation of human cortical spheroids (hCSs)**—Spheroids were generated from hESCs.<sup>48,49,97</sup> Briefly, hESCs were cultured on irradiated mouse embryonic fibroblasts (MEFs) (Gibco A34180) in hESC medium (hESCM) containing DMEM-F12, 20% knockout serum replacement (Gibco), 1% NEAA, 1% Glutamax and bFGF (10 ng/mL). The colonies were detached from the MEFs with Dispase (Millipore SCM133) and subsequently transferred into ultra-low attachment plates in neural differentiation medium containing hESCM, 10 µM SB431542 (SB), and 1 mM Dorsomorphin (DM) with ROCK inhibitor Thiazovivin (0.5 µM).<sup>49</sup> After 24 h, the medium was replaced with neural differentiation medium without Thiazovivin. The ROCK inhibitor Thiazovivin (0.5 µM) was added for the first 24 h and then removed. On day 6, the medium was replaced with serum-free neural medium (NM) containing Neurobasal medium (Gibco 10888), 2% B27 without vitamin A, 1% GlutaMAX, and 1% P/S, and supplemented with bFGF (20 ng/mL) and EGF (20 ng/mL). On day 25, bFGF and EGF were replaced with BDNF (brain-derived neurotrophic factor) and NT3 (20 ng/mL each, Peprotech). From day 43 onwards, the spheroids were cultured in NM without growth factors. Media was replaced every day from day 1 to day 9, every other day from day 9 to day 25, every 3 days from day 25 to day 43 and every four to five days from day 43 onward.

**Cryosectioning of spheroids and immunohistochemistry**—Human cortical spheroids (hCSs) were fixed with 4% PFA in PBS at 4°C overnight and then washed thoroughly with PBS, transferred to 30% sucrose, and incubated at 4°C for 72 h. Subsequently, spheroids were embedded in OCT compound, snap-frozen in an ethanol/dry ice mixture and stored at -80°C. For immunohistochemistry, the embedded spheroids were sectioned (10–20 µm) with Leica cryostat and mounted onto Superfrost Plus slides.

Spheroid sections were washed with PBS to remove OCT and blocked in 10% normal goat serum (NGS) or normal donkey serum (NDS) diluted in PBS-0.3% Triton, for 1 h at room temperature. The sections were then incubated overnight at 4°C with primary antibodies (Key resources table) diluted in PBS-0.1% Triton containing 10% NGS or NDS. On the second day, the cryosections were rinsed with PBS and incubated for 1 h with secondary antibodies diluted in PBS-0.1% Triton containing 10% NGS or NDS. Nuclei were counterstained with Hoechst 33258 (Life Technologies). Cryosections were mounted with cover glass using Vectashield antifade mounting medium. Images were collected on a Leica confocal laser-scanning (TCS SP5) microscope. For measuring synaptic size and density,

spheroid sections were immunostained with pre-/post-synaptic marker antibodies (see Key resources table) with appropriate secondary fluorescent antibodies (see Key resources table). Images were acquired with a Leica TCS SP5 confocal microscope with 405, 488, 563, and 647 nm laser lines using a 63 $\times$  immersion oil objective, with the pinhole adjusted to 1.0 Airy units. Multichannel images were acquired sequentially with identical settings applied to all samples in an experiment. Synapse-dense areas below the superficial layer of spheroids was imaged over a depth of 15  $\mu\text{m}$  z stack range. For synapses quantification, puncta were identified by intensity threshold and size thresholding in ImageJ and selected as the region of interest (ROI). ROIs were measured with the ‘Analyze particles’ plugin. The number of Synapsin 1 puncta and overlapping Synapsin 1/Homer1 puncta were quantified, and the relative density was calculated as the number of puncta per area. For puncta size analysis, only full volume puncta captured were selected from slices of z stack reconstructed confocal sections, and the puncta size was measured on a projected image stack. The quantitative data are derived from 3 independent spheroid cultures. The experimenter was blind to the genotypes and conditions in all analyses.

**Dissociation and culturing of hCSs**—Human cortical spheroids (hCSs) were chopped and incubated in 40 U/mL papain (Worthington) enzyme solution at 34–35°C for 60–90 min.<sup>49</sup> After digestion, cell clumps were washed with soybean protease inhibitor (Sigma) solution and triturated to achieve a single cell suspension. Cells were plated on glass coverslips coated with poly-L-ornithine and laminin and grown in neural medium supplemented with BDNF (20 ng/mL), NT3 (20 ng/mL) and HBEGF (5 ng/mL) for 11 days. The Rock inhibitor Thiazovivin (0.5  $\mu\text{M}$ ) was added upon plating. Half volume of medium was replaced every 3 days. To trace the morphology of single neurons or astrocytes, the culture was transfected with CaMKII-EGFP or GFAP-GFP, respectively, on day 8 of culturing and fixed on day 11.

**Immunopanning**—For immunopanning of long-term spheroid cultures, spheroids were first dissociated.<sup>48</sup> hCSs were chopped and incubated in 40 U/mL papain (Worthington) enzyme solution at a 35°C incubator with 5% CO<sub>2</sub> for 80–90 min, washed with Ovomucoid protease inhibitor (Worthington) solution, and triturated to a single cell suspension. Cells were then added to plastic petri dishes pre-coated with HepaCAM (R&D, MAB4108) (1:120 in 0.2% BSA in PBS) and incubated for 20–30 min at room temperature to allow HepaCAM-positive (astrocytes) cells to bind to the plates.<sup>11</sup> Unbound cells were transferred to a falcon tube, while the dishes with bound cells were rinsed eight times with PBS to wash away loosely bound cells. The unbound cells from washing were combined into a falcon tube, centrifuged, and cultured on poly-L-ornithine coated coverslips (neuron-enriched cultures). For RNA collection of purified astrocytes, bound cells were scraped off the immunopanning dish directly with TRIzol reagent. For all other analyses requiring culturing, bound astrocytes were incubated in trypsin solution for 10–15 min at 37°C, then rinsed off the plates, centrifuged and cultured on Matrigel coated 96-well plates or coverslips.

Purified astrocytes were maintained in medium containing 50% Neurobasal-A medium, 50% DMEM, 1% P/S, 2% B27, 0.5% Glutamax, and 5 ng/mL HBEGF.<sup>48</sup> Neuron-enriched cultures were maintained in neural medium containing 50 ng/mL BDNF and 20 ng/mL

NT3.<sup>11</sup> Rock inhibitor Thiazovivin (0.5 μM) was added upon plating of neurons and astrocytes and removed with complete medium change on day 2. From day 2 onward, half medium was replaced with a fresh medium every 3 days. The astrocytes were used after 7 days in culture for glutamate uptake and MitoSOX assays. For <sup>1</sup>H- NMR analysis of extracellular metabolites, astrocyte conditioned media (ACM) and neuron conditioned media (NCM) were collected on day 5 and day 8 of culturing upon replacing of media, combined, centrifuged at 2000g for 5 min, and stored at -80°C. To trace the morphology of single astrocytes, the purified astrocytes cultured on coverslips were transfected with GFAP-GFP on day 8 and fixed on day 11.

**Immunohistochemistry of human postmortem brain tissue**—Postmortem brain tissues were received in 10% formalin, dehydrated with ethanol (30%–100%), cleared with xylene, embedded in paraffin, and sectioned at 10 μm thickness with microtome. Sections were dried, deparaffined with xylene and rehydrated with ethanol (100%–70%) and then with water according to standard protocols. Antigen retrieval was performed in 10 mM sodium citrate, pH 6.0 and 0.02% Triton X-100, in a pressure cooker for 10 min. Sections were permeabilized and blocked with 5% donkey serum in PBS-0.1% Triton, incubated overnight at 4°C with rabbit anti-GFAP primary antibody followed by incubation at room temperature for 1 h with a secondary fluorescence conjugated-antibody.

## QUANTIFICATION AND STATISTICAL ANALYSIS

All experiments were performed with at least three biological replicates. Except for the RNA sequencing, all statistical analyses were performed using Excel or Prism 9 (GraphPad) software. The statistical details of experiments are also present in the figure legends. Data are presented as mean ± s.e.m. Significance was defined by p < 0.05, \*; p < 0.01, \*\*; p < 0.001, \*\*\*; not significant, ns.

## Supplementary Material

Refer to Web version on PubMed Central for supplementary material.

## ACKNOWLEDGMENTS

The authors thank Drs. Markus Riessland and Sian Piret for guidance in mitochondrial assays; Drs. Shaoyu Ge and Gregory Kirschen for guidance in transplantation experiments; Dr. Martine Ziliox for guidance in NMR analysis; Dr. Chun-Li Zhang for sharing the GFAP-EGFP plasmid; Sulan Xu for guidance in immunostaining of postmortem human brains; Christina Rodrigues, Ron Lev, Chana Rosenzweig, and Samuel Khoo for technical assistance; NIH NeuroBioBank, Olivia Spicer (NIH/NIMH), and Alexandra LeFevre (UMB Brain and Tissue Bank) for assisting and providing postmortem brain tissues; and CPRIT Proteomics and Metabolomics Core Facility for targeted mass spectrometry analysis. Supported by grants from the National Institutes of Health (R01HD081037 and R21MH126381 to N.B.; R01GM120033 to M.M.S.; R01DK121970 to F.L.; P30CA125123 and P50HD103555 to B.C.M.), CPRIT RP170005 Proteomics and Metabolomics Core Facility, BCM Advanced Technology Core support of NMR and Drug Metabolism Core (to L.M. and F.L.), the Cynthia and Antony Petrello Endowment (to M.M.S.), and the Rett Syndrome Research Trust (to N.B.).

## REFERENCES

- Carney RM, Wolpert CM, Ravan SA, Shahbazian M, Ashley-Koch A, Cuccaro ML, Vance JM, and Pericak-Vance MA (2003). Identification of MeCP2 mutations in a series of females with autistic disorder. *Pediatr. Neurol.* 28, 205–211. 10.1016/s0887-8994(02)00624-0. [PubMed: 12770674]

2. Cohen D, Lazar G, Couvert P, Desportes V, Lippe D, Mazet P, and Héron D (2002). MECP2 mutation in a boy with language disorder and schizophrenia. *Am. J. Psychiatry* 159, 148–149. 10.1176/appi.ajp.159.1.148-a.
3. Chahrour M, and Zoghbi HY (2007). The story of Rett syndrome: from clinic to neurobiology. *Neuron* 56, 422–437. 10.1016/j.neuron.2007.10.001. [PubMed: 17988628]
4. Amir RE, Van den Veyver IB, Wan M, Tran CQ, Francke U, and Zoghbi HY (1999). Rett syndrome is caused by mutations in X-linked MECP2, encoding methyl-CpG-binding protein 2. *Nat. Genet.* 23, 185–188. 10.1038/13810. [PubMed: 10508514]
5. Ballas N, Liou DT, Grunseich C, and Mandel G (2009). Non-cell autonomous influence of MeCP2-deficient glia on neuronal dendritic morphology. *Nat. Neurosci.* 12, 311–317. 10.1038/nn.2275. [PubMed: 19234456]
6. Maezawa I, Swanberg S, Harvey D, LaSalle JM, and Jin LW (2009). Rett syndrome astrocytes are abnormal and spread MeCP2 deficiency through gap junctions. *J. Neurosci.* 29, 5051–5061. 10.1523/JNEUROSCI.0324-09.2009. [PubMed: 19386901]
7. Liou DT, Garg SK, Monaghan CE, Raber J, Foust KD, Kaspar BK, Hirrlinger PG, Kirchhoff F, Bissonnette JM, Ballas N, and Mandel G (2011). A role for glia in the progression of Rett's syndrome. *Nature* 475, 497–500. 10.1038/nature10214. [PubMed: 21716289]
8. Nguyen MVC, Felice CA, Du F, Covey MV, Robinson JK, Mandel G, and Ballas N (2013). Oligodendrocyte lineage cells contribute unique features to Rett syndrome neuropathology. *J. Neurosci.* 33, 18764–18774. 10.1523/JNEUROSCI.2657-13.2013. [PubMed: 24285883]
9. Williams EC, Zhong X, Mohamed A, Li R, Liu Y, Dong Q, Ananiev GE, Mok JCC, Lin BR, Lu J, et al. (2014). Mutant astrocytes differentiated from Rett syndrome patients-specific iPSCs have adverse effects on wild-type neurons. *Hum. Mol. Genet.* 23, 2968–2980. 10.1093/hmg/ddu008. [PubMed: 24419315]
10. Oberheim NA, Takano T, Han X, He W, Lin JHC, Wang F, Xu Q, Wyatt JD, Pilcher W, Ojemann JG, et al. (2009). Uniquely hominid features of adult human astrocytes. *J. Neurosci.* 29, 3276–3287. 10.1523/JNEUROSCI.4707-08.2009. [PubMed: 19279265]
11. Zhang Y, Sloan SA, Clarke LE, Caneda C, Plaza CA, Blumenthal PD, Vogel H, Steinberg GK, Edwards MSB, Li G, et al. (2016). Purification and characterization of progenitor and mature human astrocytes reveals transcriptional and functional differences with mouse. *Neuron* 89, 37–53. 10.1016/j.neuron.2015.11.013. [PubMed: 26687838]
12. Vasile F, Dossi E, and Rouach N (2017). Human astrocytes: structure and functions in the healthy brain. *Brain Struct. Funct.* 222, 2017–2029. 10.1007/s00429-017-1383-5. [PubMed: 28280934]
13. Miller JA, Horvath S, and Geschwind DH (2010). Divergence of human and mouse brain transcriptome highlights Alzheimer disease pathways. *Proc. Natl. Acad. Sci. USA* 107, 12698–12703. 10.1073/pnas.0914257107. [PubMed: 20616000]
14. Li J, Pan L, Pembroke WG, Rexach JE, Godoy MI, Condron MC, Alvarado AG, Harteni M, Chen YW, Stiles L, et al. (2021). Conservation and divergence of vulnerability and responses to stressors between human and mouse astrocytes. *Nat. Commun.* 12, 3958. 10.1038/s41467-021-24232-3. [PubMed: 34172753]
15. Yang Y, Higashimori H, and Morel L (2013). Developmental maturation of astrocytes and pathogenesis of neurodevelopmental disorders. *J. Neurodev. Disord.* 5, 22. 10.1186/1866-1955-5-22. [PubMed: 23988237]
16. Hasel P, Dando O, Jiwaji Z, Baxter P, Todd AC, Heron S, Márkus NM, McQueen J, Hampton DW, Torvell M, et al. (2017). Neurons and neuronal activity control gene expression in astrocytes to regulate their development and metabolism. *Nat. Commun.* 8, 15132. 10.1038/ncomms15132. [PubMed: 28462931]
17. McGann JC, and Mandel G (2018). Neuronal activity induces glutathione metabolism gene expression in astrocytes. *Glia* 66, 2024–2039. 10.1002/glia.23455. [PubMed: 30043519]
18. Schiweck J, Eickholt BJ, and Murk K (2018). Important shapeshifter: mechanisms allowing astrocytes to respond to the changing nervous system during development, injury and disease. *Front. Cell. Neurosci.* 12, 261. 10.3389/fncel.2018.00261. [PubMed: 30186118]

19. Kim TG, Yao R, Monnell T, Cho JH, Vasudevan A, Koh A, Peeyush KT, Moon M, Datta D, Bolshakov VY, et al. (2014). Efficient specification of interneurons from human pluripotent stem cells by dorsoventral and rostrocaudal modulation. *Stem Cell*. 32, 1789–1804. 10.1002/stem.1704.
20. Mekhoubad S, Bock C, de Boer AS, Kiskinis E, Meissner A, and Eggan K (2012). Erosion of dosage compensation impacts human iPSC disease modeling. *Cell Stem Cell* 10, 595–609. 10.1016/j.stem.2012.02.014. [PubMed: 22560080]
21. Li Y, Wang H, Muffat J, Cheng AW, Orlando DA, Lovén J, Kwok SM, Feldman DA, Bateup HS, Gao Q, et al. (2013). Global transcriptional and translational repression in human-embryonic-stem-cell-derived Rett syndrome neurons. *Cell Stem Cell* 13, 446–458. 10.1016/j.stem.2013.09.001. [PubMed: 24094325]
22. Anguera MC, Sadreyev R, Zhang Z, Szanto A, Payer B, Sheridan SD, Kwok S, Haggarty SJ, Sur M, Alvarez J, et al. (2012). Molecular signatures of human induced pluripotent stem cells highlight sex differences and cancer genes. *Cell Stem Cell* 11, 75–90. 10.1016/j.stem.2012.03.008. [PubMed: 22770242]
23. Xiang Y, Tanaka Y, Patterson B, Hwang SM, Hysolli E, Cakir B, Kim KY, Wang W, Kang YJ, Clement EM, et al. (2020). Dysregulation of BRD4 function underlies the functional abnormalities of MeCP2 mutant neurons. *Mol. Cell* 79, 84–98.e9. 10.1016/j.molcel.2020.05.016. [PubMed: 32526163]
24. Krishnaraj R, Ho G, and Christodoulou J (2017). RettBASE: Rett syndrome database update. *Hum. Mutat.* 38, 922–931. 10.1002/humu.23263. [PubMed: 28544139]
25. Cuddapah VA, Pillai RB, Shekar KV, Lane JB, Motil KJ, Skinner SA, Tarquinio DC, Glaze DG, McGwin G, Kaufmann WE, et al. (2014). Methyl-CpG-binding protein 2 (MECP2) mutation type is associated with disease severity in Rett syndrome. *J. Med. Genet.* 51, 152–158. 10.1136/jmedgenet-2013-102113. [PubMed: 24399845]
26. Neul JL, Fang P, Barrish J, Lane J, Caeg EB, Smith EO, Zoghbi H, Percy A, and Glaze DG (2008). Specific mutations in methyl-CpG-binding protein 2 confer different severity in Rett syndrome. *Neurology* 70, 1313–1321. 10.1212/01.wnl.0000291011.54508.aa. [PubMed: 18337588]
27. Liu Y, Han SSW, Wu Y, Tuohy TMF, Xue H, Cai J, Back SA, Sherman LS, Fischer I, and Rao MS (2004). CD44 expression identifies astrocyte-restricted precursor cells. *Dev. Biol.* 276, 31–46. 10.1016/j.ydbio.2004.08.018. [PubMed: 15531362]
28. Sun W, Cornwell A, Li J, Peng S, Osorio MJ, Aalling N, Wang S, Benraiss A, Lou N, Goldman SA, and Nedergaard M (2017). SOX9 is an astrocyte-specific nuclear marker in the adult brain outside the neurogenic regions. *J. Neurosci.* 37, 4493–4507. 10.1523/JNEUROSCI.3199-16.2017. [PubMed: 28336567]
29. Jiang P, Chen C, Liu XB, Pleasure DE, Liu Y, and Deng W (2016). Human iPSC-derived immature astroglia promote oligodendrogenesis by increasing TIMP-1 secretion. *Cell Rep.* 15, 1303–1315. 10.1016/j.celrep.2016.04.011. [PubMed: 27134175]
30. Escartin C, Galea E, Lakatos A, O'Callaghan JP, Petzold GC, Serrano-Pozo A, Steinhäuser C, Volterra A, Carmignoto G, Agarwal A, et al. (2021). Reactive astrocyte nomenclature, definitions, and future directions. *Nat. Neurosci.* 24, 312–325. 10.1038/s41593-020-00783-4. [PubMed: 33589835]
31. Bélanger M, Allaman I, and Magistretti PJ (2011). Brain energy metabolism: focus on astrocyte-neuron metabolic cooperation. *Cell Metab.* 14, 724–738. 10.1016/j.cmet.2011.08.016. [PubMed: 22152301]
32. Weber B, and Barros LF (2015). The astrocyte: powerhouse and recycling center. *Cold Spring Harb. Perspect. Biol.* 7, a020396. 10.1101/cspperspect.a020396. [PubMed: 25680832]
33. Patel DC, Tewari BP, Chaunsali L, and Sontheimer H (2019). Neuron-glia interactions in the pathophysiology of epilepsy. *Nat. Rev. Neurosci.* 20, 282–297. 10.1038/s41583-019-0126-4. [PubMed: 30792501]
34. Rose J, Brian C, Pappa A, Panayiotidis MI, and Franco R (2020). Mitochondrial metabolism in astrocytes regulates brain bioenergetics, neurotransmission and redox balance. *Front. Neurosci.* 14, 536682. 10.3389/fnins.2020.536682. [PubMed: 33224019]
35. De Filippis B, Fabbri A, Simone D, Canese R, Ricceri L, MalchiodiAlbedi F, Laviola G, and Fiorentini C (2012). Modulation of RhoGTPases improves the behavioral phenotype and reverses

- astrocytic deficits in a mouse model of Rett syndrome. *Neuropsychopharmacology* 37, 1152–1163. 10.1038/npp.2011.301. [PubMed: 22157810]
36. Bebensee DF, Can K, and Müller M (2017). Increased mitochondrial mass and cytosolic redox imbalance in hippocampal astrocytes of a mouse model of Rett syndrome: subcellular changes revealed by ratiometric imaging of JC-1 and roGFP1 fluorescence. *Oxid. Med. Cell. Longev.* 2017, 3064016. 10.1155/2017/3064016. [PubMed: 28894505]
37. Müller M, and Can K (2014). Aberrant redox homoeostasis and mitochondrial dysfunction in Rett syndrome. *Biochem. Soc. Trans.* 42, 959–964. 10.1042/BST20140071. [PubMed: 25109986]
38. Kriaucionis S, Paterson A, Curtis J, Guy J, Macleod N, and Bird A (2006). Gene expression analysis exposes mitochondrial abnormalities in a mouse model of Rett syndrome. *Mol. Cell Biol.* 26, 5033–5042. 10.1128/MCB.01665-05. [PubMed: 16782889]
39. Rogatzki MJ, Ferguson BS, Goodwin ML, and Gladden LB (2015). Lactate is always the end product of glycolysis. *Front. Neurosci.* 9, 22. 10.3389/fnins.2015.00022. [PubMed: 25774123]
40. Magistretti PJ, and Allaman I (2018). Lactate in the brain: from metabolic end-product to signalling molecule. *Nat. Rev. Neurosci.* 19, 235–249. 10.1038/nrn.2018.19. [PubMed: 29515192]
41. Zhang SY, Dong YQ, Wang P, Zhang X, Yan Y, Sun L, Liu B, Zhang D, Zhang H, Liu H, et al. (2018). Adipocyte-derived lysophosphatidylcholine activates adipocyte and adipose tissue macrophage nod-like receptor protein 3 inflammasomes mediating homocysteine-induced insulin resistance. *EBioMedicine* 31, 202–216. 10.1016/j.ebiom.2018.04.022. [PubMed: 29735414]
42. Law SH, Chan ML, Marathe GK, Parveen F, Chen CH, and Ke LY (2019). An updated Review of lysophosphatidylcholine metabolism in human diseases. *Int. J. Mol. Sci.* 20, 1149. 10.3390/ijms20051149. [PubMed: 30845751]
43. Rabinovitch RC, Samborska B, Faubert B, Ma EH, Gravel SP, Andrzejewski S, Raissi TC, Pause A, St-Pierre J, and Jones RG (2017). AMPK maintains cellular metabolic homeostasis through regulation of mitochondrial reactive oxygen species. *Cell Rep.* 21, 1–9. 10.1016/j.celrep.2017.09.026. [PubMed: 28978464]
44. Bak LK, Schousboe A, and Waagepetersen HS (2006). The glutamate/GABA-glutamine cycle: aspects of transport, neurotransmitter homeostasis and ammonia transfer. *J. Neurochem.* 98, 641–653. 10.1111/j.1471-4159.2006.03913.x. [PubMed: 16787421]
45. Clarke LE, and Barres BA (2013). Emerging roles of astrocytes in neuralcircuit development. *Nat. Rev. Neurosci.* 14, 311–321. 10.1038/nrn3484. [PubMed: 23595014]
46. Han X, Chen M, Wang F, Windrem M, Wang S, Shanz S, Xu Q, Oberheim NA, Bekar L, Betstadt S, et al. (2013). Forebrain engraftment by human glial progenitor cells enhances synaptic plasticity and learning in adult mice. *Cell Stem Cell* 12, 342–353. 10.1016/j.stem.2012.12.015. [PubMed: 23472873]
47. Ullian EM, Sapperstein SK, Christopherson KS, and Barres BA (2001). Control of synapse number by glia. *Science* 291, 657–661. 10.1126/science.291.5504.657. [PubMed: 11158678]
48. Sloan SA, Darmanis S, Huber N, Khan TA, Birey F, Caneda C, Reimer R, Quake SR, Barres BA, and Pasqua SP (2017). Human astrocyte maturation captured in 3D cerebral cortical spheroids derived from pluripotent stem cells. *Neuron* 95, 779–790.e6. 10.1016/j.neuron.2017.07.035. [PubMed: 28817799]
49. Sloan SA, Andersen J, Pa ca AM, Birey F, and Pa ca SP (2018). Generation and assembly of human brain region-specific three-dimensional cultures. *Nat. Protoc.* 13, 2062–2085. 10.1038/s41596-018-0032-7. [PubMed: 30202107]
50. Chen RZ, Akbarian S, Tudor M, and Jaenisch R (2001). Deficiency of methyl-CpG binding protein-2 in CNS neurons results in a Rett-like phenotype in mice. *Nat. Genet.* 27, 327–331. 10.1038/85906. [PubMed: 11242118]
51. Zoghbi HY (2016). Rett syndrome and the ongoing legacy of close clinical observation. *Cell* 167, 293–297. 10.1016/j.cell.2016.09.039. [PubMed: 27716498]
52. Yazdani M, Deogracias R, Guy J, Poot RA, Bird A, and Barde YA (2012). Disease modeling using embryonic stem cells: MeCP2 regulates nuclear size and RNA synthesis in neurons. *Stem Cell*. 30, 2128–2139. 10.1002/stem.1180.

53. Du F, Nguyen MVC, Karten A, Felice CA, Mandel G, and Ballas N (2016). Acute and crucial requirement for MeCP2 function upon transition from early to late adult stages of brain maturation. *Hum. Mol. Genet.* 25, 1690–1702. 10.1093/hmg/ddw038. [PubMed: 26908602]
54. Walz W, and Mukerji S (1988). Lactate release from cultured astrocytes and neurons: a comparison. *Glia* 1, 366–370. 10.1002/glia.440010603. [PubMed: 2976396]
55. Burke EE, Chenoweth JG, Shin JH, Collado-Torres L, Kim SK, Micali N, Wang Y, Colantuoni C, Straub RE, Hoeppner DJ, et al. (2020). Dissecting transcriptomic signatures of neuronal differentiation and maturation using iPSCs. *Nat. Commun.* 11, 462. 10.1038/s41467-019-14266-z. [PubMed: 31974374]
56. Kierans SJ, and Taylor CT (2021). Regulation of glycolysis by the hypoxia-inducible factor (HIF): implications for cellular physiology. *J. Physiol.* 599, 23–37. 10.1113/JP280572. [PubMed: 33006160]
57. Haas RH, Nasirian F, Hua X, Nakano K, and Hennessy M (1995). Oxidative metabolism in Rett syndrome: 2. Biochemical and molecular studies. *Neuropediatrics* 26, 95–99. 10.1055/s-2007-979735. [PubMed: 7566465]
58. Lappalainen R, and Riikonen RS (1994). Elevated CSF lactate in the Rett syndrome: cause or consequence? *Brain Dev.* 16, 399–401. 10.1016/0387-7604(94)90129-5. [PubMed: 7892961]
59. Matsuishi T, Urabe F, Komori H, Yamashita Y, Naito E, Kuroda Y, Horikawa M, and Ohtaki E (1992). The Rett syndrome and CSF lactic acid patterns. *Brain Dev.* 14, 68–70. 10.1016/s0387-7604(12)80283-x. [PubMed: 1590531]
60. Barros LF, and Weber B (2018). CrossTalk proposal: an important astrocyte-to-neuron lactate shuttle couples neuronal activity to glucose utilisation in the brain. *J. Physiol.* 596, 347–350. 10.1113/JP274944. [PubMed: 29292516]
61. Margineanu MB, Mahmood H, Fiumelli H, and Magistretti PJ (2018). L-lactate regulates the expression of synaptic plasticity and neuroprotection genes in cortical neurons: a transcriptome analysis. *Front. Mol. Neurosci.* 11, 375. 10.3389/fnmol.2018.00375. [PubMed: 30364173]
62. Schousboe A, Scafidi S, Bak LK, Waagepetersen HS, and McKenna MC (2014). Glutamate metabolism in the brain focusing on astrocytes. *Adv. Neurobiol.* 11, 13–30. 10.1007/978-3-319-08894-5\_2. [PubMed: 25236722]
63. Mahmoud S, Gharagozloo M, Simard C, and Gris D (2019). Astrocytes maintain glutamate homeostasis in the CNS by controlling the balance between glutamate uptake and release. *Cells* 8, 184. 10.3390/cells8020184. [PubMed: 30791579]
64. Voloboueva LA, Suh SW, Swanson RA, and Giffard RG (2007). Inhibition of mitochondrial function in astrocytes: implications for neuroprotection. *J. Neurochem.* 102, 1383–1394. 10.1111/j.14714159.2007.04634.x. [PubMed: 17488276]
65. Bantle CM, Hirst WD, Weihofen A, and Shlevkov E (2020). Mitochondrial dysfunction in astrocytes: a role in Parkinson's disease? *Front. Cell Dev. Biol.* 8, 608026. 10.3389/fcell.2020.608026. [PubMed: 33537300]
66. Calfa G, Hablitz JJ, and Pozzo-Miller L (2011). Network hyperexcitability in hippocampal slices from Mecp2 mutant mice revealed by voltage-sensitive dye imaging. *J. Neurophysiol.* 105, 1768–1784. 10.1152/jn.00800.2010. [PubMed: 21307327]
67. Calfa G, Li W, Rutherford JM, and Pozzo-Miller L (2015). Excitation/inhibition imbalance and impaired synaptic inhibition in hippocampal area CA3 of Mecp2 knockout mice. *Hippocampus* 25, 159–168. 10.1002/hipo.22360. [PubMed: 25209930]
68. Zhang W, Peterson M, Beyer B, Frankel WN, and Zhang ZW (2014). Loss of MeCP2 from forebrain excitatory neurons leads to cortical hyperexcitation and seizures. *J. Neurosci.* 34, 2754–2763. 10.1523/JNEUROSCI.4900-12.2014. [PubMed: 24523563]
69. Sies H, and Jones DP (2020). Reactive oxygen species (ROS) as pleiotropic physiological signalling agents. *Nat. Rev. Mol. Cell Biol.* 21, 363–383. 10.1038/s41580-020-0230-3. [PubMed: 32231263]
70. Adebayo OL, Dewenter I, Rinne L, Golubiani G, Solomonia R, and Müller M (2020). RETRACTED: intensified mitochondrial hydrogen peroxide release occurs in all brain regions, affects male as well as female Rett mice, and constitutes a life-long burden. *Arch. Biochem. Biophys.* 696, 108666. 10.1016/j.abb.2020.108666. [PubMed: 33160914]

71. De Felice C, Ciccoli L, Leoncini S, Signorini C, Rossi M, Vannuccini L, Guazzi G, Latini G, Comporti M, Valacchi G, and Hayek J (2009). Systemic oxidative stress in classic Rett syndrome. *Free Radic. Biol. Med.* 47, 440–448. 10.1016/j.freeradbiomed.2009.05.016. [PubMed: 19464363]
72. Muller M (2019). Disturbed redox homeostasis and oxidative stress: potential players in the developmental regression in Rett syndrome. *Neurosci. Biobehav. Rev.* 98, 154–163. 10.1016/j.neubiorev.2018.12.009. [PubMed: 30639673]
73. Squillaro T, Alessio N, Capasso S, Di Bernardo G, Melone MAB, Peluso G, and Galderisi U (2019). Senescence phenomena and metabolic alteration in mesenchymal stromal cells from a mouse model of Rett syndrome. *Int. J. Mol. Sci.* 20, 2508. 10.3390/ijms20102508. [PubMed: 31117273]
74. Filosa S, Pecorelli A, D'Esposito M, Valacchi G, and Hajek J (2015). Exploring the possible link between MeCP2 and oxidative stress in Rett syndrome. *Free Radic. Biol. Med.* 88, 81–90. 10.1016/j.freeradbiomed.2015.04.019. [PubMed: 25960047]
75. Shulyakova N, Andreazza AC, Mills LR, and Eubanks JH (2017). Mitochondrial dysfunction in the pathogenesis of Rett syndrome: implications for mitochondria-targeted therapies. *Front. Cell. Neurosci.* 11, 58. 10.3389/fncel.2017.00058. [PubMed: 28352216]
76. Nguyen MVC, Du F, Felice CA, Shan X, Nigam A, Mandel G, Robinson JK, and Ballas N (2012). MeCP2 is critical for maintaining mature neuronal networks and global brain anatomy during late stages of postnatal brain development and in the mature adult brain. *J. Neurosci.* 32, 10021–10034. 10.1523/JNEUROSCI.1316-12.2012. [PubMed: 22815516]
77. Pacheco NL, Heaven MR, Holt LM, Crossman DK, Boggio KJ, Shaffer SA, Flint DL, and Olsen ML (2017). RNA sequencing and proteomics approaches reveal novel deficits in the cortex of MeCP2-deficient mice, a model for Rett syndrome. *Mol. Autism.* 8, 56. 10.1186/s13229-017-0174-4. [PubMed: 29090078]
78. Potokar M, Morita M, Wiche G, and Jorgacevski J (2020). The diversity of intermediate filaments in astrocytes. *Cells* 9. 10.3390/cells9071604.
79. Allen NJ, and Eroglu C (2017). Cell biology of astrocyte-synapse interactions. *Neuron* 96, 697–708. 10.1016/j.neuron.2017.09.056. [PubMed: 29096081]
80. Kim KY, Hysolli E, and Park IH (2011). Neuronal maturation defect in induced pluripotent stem cells from patients with Rett syndrome. *Proc. Natl. Acad. Sci. USA* 108, 14169–14174. 10.1073/pnas.1018979108. [PubMed: 21807996]
81. Palm T, Bolognin S, Meiser J, Nickels S, Träger C, Meilenbrock RL, Brockhaus J, Schreitmüller M, Missler M, and Schwamborn JC (2015). Rapid and robust generation of long-term self-renewing human neural stem cells with the ability to generate mature astroglia. *Sci. Rep.* 5, 16321. 10.1038/srep16321. [PubMed: 26541394]
82. Bardy C, van den Hurk M, Eames T, Marchand C, Hernandez RV, Kellogg M, Gorris M, Galet B, Palomares V, Brown J, et al. (2015). Neuronal medium that supports basic synaptic functions and activity of human neurons in vitro. *Proc. Natl. Acad. Sci. USA* 112, E2725–E2734. 10.1073/pnas.1504393112. [PubMed: 25870293]
83. Dobin A, Davis CA, Schlesinger F, Drenkow J, Zaleski C, Jha S, Batut P, Chaisson M, and Gingeras TR (2013). STAR: ultrafast universal RNA-seq aligner. *Bioinformatics* 29, 15–21. 10.1093/bioinformatics/bts635. [PubMed: 23104886]
84. Love MI, Huber W, and Anders S (2014). Moderated estimation of fold change and dispersion for RNA-seq data with DESeq2. *Genome Biol.* 15, 550. 10.1186/s13059-014-0550-8. [PubMed: 25516281]
85. Subramanian A, Tamayo P, Mootha VK, Mukherjee S, Ebert BL, Gillette MA, Paulovich A, Pomeroy SL, Golub TR, Lander ES, and Mesirov JP (2005). Gene set enrichment analysis: a knowledge-based approach for interpreting genome-wide expression profiles. *Proc. Natl. Acad. Sci. USA* 102, 15545–15550. 10.1073/pnas.0506580102. [PubMed: 16199517]
86. Huang DW, Sherman BT, and Lempicki RA (2009). Systematic and integrative analysis of large gene lists using DAVID bioinformatics resources. *Nat. Protoc.* 4, 44–57. 10.1038/nprot.2008.211. [PubMed: 19131956]

87. Huang DW, Sherman BT, and Lempicki RA (2009). Bioinformatics enrichment tools: paths toward the comprehensive functional analysis of large gene lists. *Nucleic Acids Res.* 37, 1–13. 10.1093/nar/gkn923. [PubMed: 19033363]
88. Putluri N, Shojaie A, Vasu VT, Vareed SK, Nalluri S, Putluri V, Thangjam GS, Panzitt K, Tallman CT, Butler C, et al. (2011). Metabolomic profiling reveals potential markers and bioprocesses altered in bladder cancer progression. *Cancer Res.* 71, 7376–7386. 10.1158/0008-5472.CAN-11-1154. [PubMed: 21990318]
89. Amara CS, Ambati CR, Vantaku V, Badrajee Piyarathna DW, Donepudi SR, Ravi SS, Arnold JM, Putluri V, Chatta G, Guru KA, et al. (2019). Serum metabolic profiling identified a distinct metabolic signature in bladder cancer smokers: a key metabolic enzyme associated with patient survival. *Cancer Epidemiol. Biomarkers Prev.* 28, 770–781. 10.1158/1055-9965.EPI-18-0936. [PubMed: 30642841]
90. Wangler MF, Chao YH, Bayat V, Giagtzoglou N, Shinde AB, Putluri N, Coarfa C, Donti T, Graham BH, Faust JE, et al. (2017). Peroxisomal biogenesis is genetically and biochemically linked to carbohydrate metabolism in *Drosophila* and mouse. *PLoS Genet.* 13, e1006825. 10.1371/journal.pgen.1006825. [PubMed: 28640802]
91. Du F, Yu Q, Chen A, Chen D, and Yan SS (2018). Astrocytes attenuate mitochondrial dysfunctions in human dopaminergic neurons derived from iPSC. *Stem Cell Rep.* 10, 366–374. 10.1016/j.stemcr.2017.12.021.
92. Liao PC, Franco-Iborra S, Yang Y, and Pon LA (2020). Live cell imaging of mitochondrial redox state in mammalian cells and yeast. *Methods Cell Biol.* 155, 295–319. 10.1016/bs.mcb.2019.11.008. [PubMed: 32183963]
93. Covey MV, Streb JW, Spektor R, and Ballas N (2012). REST regulates the pool size of the different neural lineages by restricting the generation of neurons and oligodendrocytes from neural stem/progenitor cells. *Development* 139, 2878–2890. 10.1242/dev.074765. [PubMed: 22791895]
94. Ferreira TA, Blackman AV, Oyrer J, Jayabal S, Chung AJ, Watt AJ, Sjöström PJ, and Van Meyel DJ (2014). Neuronal morphometry directly from bitmap images.
95. Kaeser PS, Deng L, Wang Y, Dulubova I, Liu X, Rizo J, and Südhof TC (2011). RIM proteins tether Ca<sup>2+</sup> channels to presynaptic active zones via a direct PDZ-domain interaction. *Cell* 144, 282–295. 10.1016/j.cell.2010.12.029. [PubMed: 21241895]
96. Windrem MS, Osipovitch M, Liu Z, Bates J, Chandler-Militello D, Zou L, Munir J, Schanz S, McCoy K, Miller RH, et al. (2017). Human iPSC glial mouse chimeras reveal glial contributions to schizophrenia. *Cell Stem Cell* 21, 195–208.e6. 10.1016/j.stem.2017.06.012. [PubMed: 28736215]
97. Paca AM, Sloan SA, Clarke LE, Tian Y, Makinson CD, Huber N, Kim CH, Park JY, O'Rourke NA, Nguyen KD, et al. (2015). Functional cortical neurons and astrocytes from human pluripotent stem cells in 3D culture. *Nat. Methods* 12, 671–678. 10.1038/nmeth.3415. [PubMed: 26005811]

### Highlights

- Human astrocytes bearing MeCP2 mutations have altered transcriptional landscape
- Mutant astrocytes have impaired energy metabolism and dysfunctional mitochondria
- Both mutant astrocytes and neurons are unable to develop normal mature morphology
- These abnormal morphologies are caused by cell- and non-cell-autonomous effects

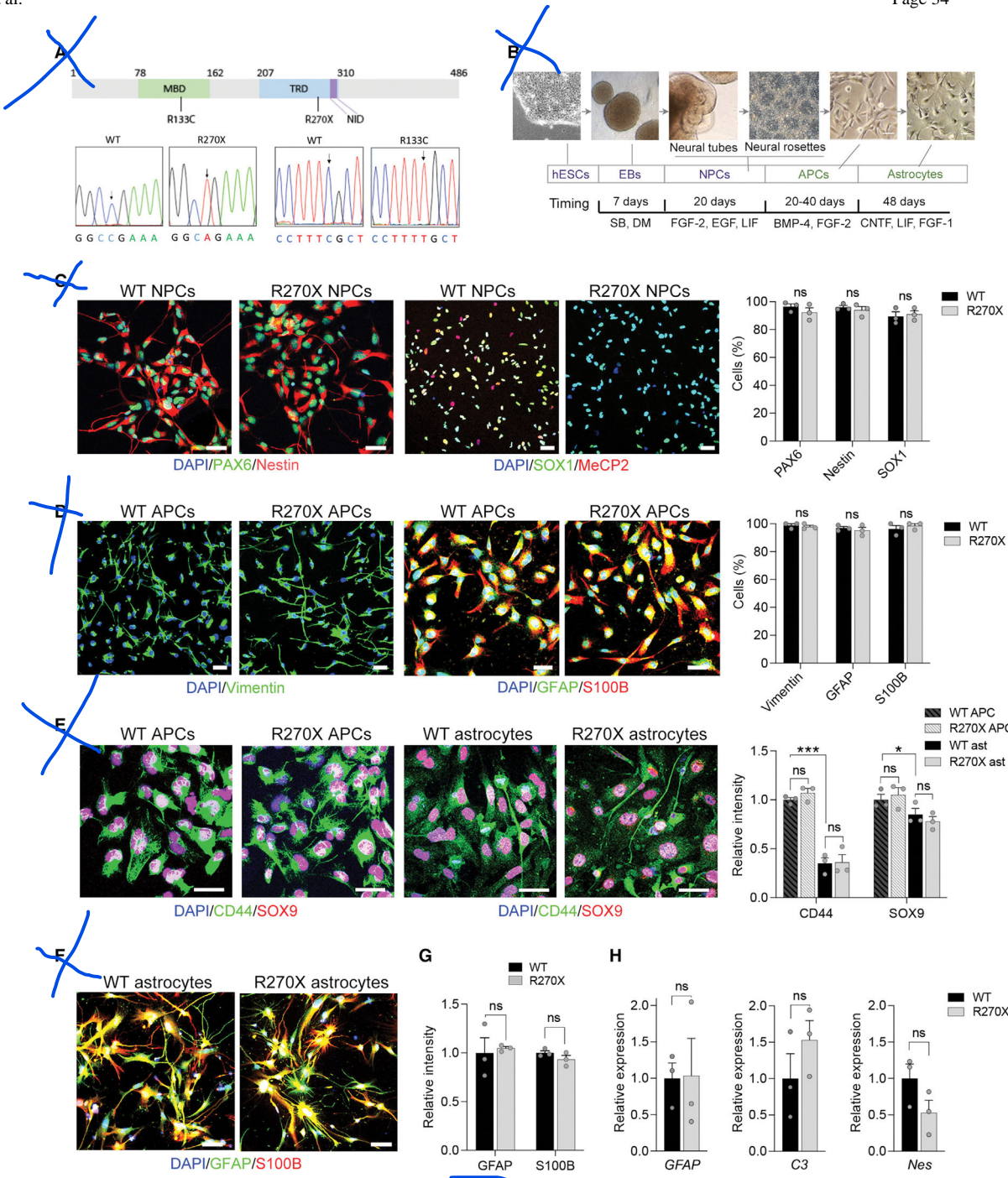


**Figure 1. Human astrocytes are generated from normal and R270X mutant ESCs with similar efficiency**

(A) (Top) Location of R270X and R133C mutations in the MeCP2 protein domains.

(Bottom) Genomic DNA sequencing of the *MECP2* regions flanking the R133C and R270X mutations in the mutant hESC lines and corresponding regions in the WT hESC lines.

Arrows mark the position of mutated nucleotides.

(B) Schematic showing the stages of differentiation from hESCs to astrocytes. EBs, embryoid bodies (STAR Methods).

(C and D) Representative confocal images (C and D, left) and quantification of cells (C and D, right) in NPC cultures expressing PAX6, Nestin, and SOX1 (C), and in APC cultures expressing Vimentin, GFAP, and S100B (D).

(E) Images (left) and immunofluorescence intensity (right) of CD44-and SOX9-expressing cells in APC and astrocyte cultures. The nuclei in magenta represent colocalized SOX9-positive cells (red) and DAPI (blue).

(F and G) Representative images (F) and immunofluorescence intensity (G) of GFAP- and S100B-expressing cells in astrocyte cultures.

(H) Relative expression of reactive astrocyte marker genes (*GFAP*, *C3*, *Nestin*) in WT and R270X-mutant astrocytes based on RNA-seq. Data points represent  $n = 3$  biological replicates, 3–5 fields per replicate (C and D), 30–36 cells per replicate (E and G). Scale bars, 50  $\mu$ m. Bars represent mean  $\pm$  standard error of the mean.

(G) Student's t tests (C, D, G, H); two-way ANOVA with Tukey post hoc analysis (E). ns, not significant. \* $p < 0.05$ , \*\*\* $p < 0.001$ . See also Figures S1 and S2.

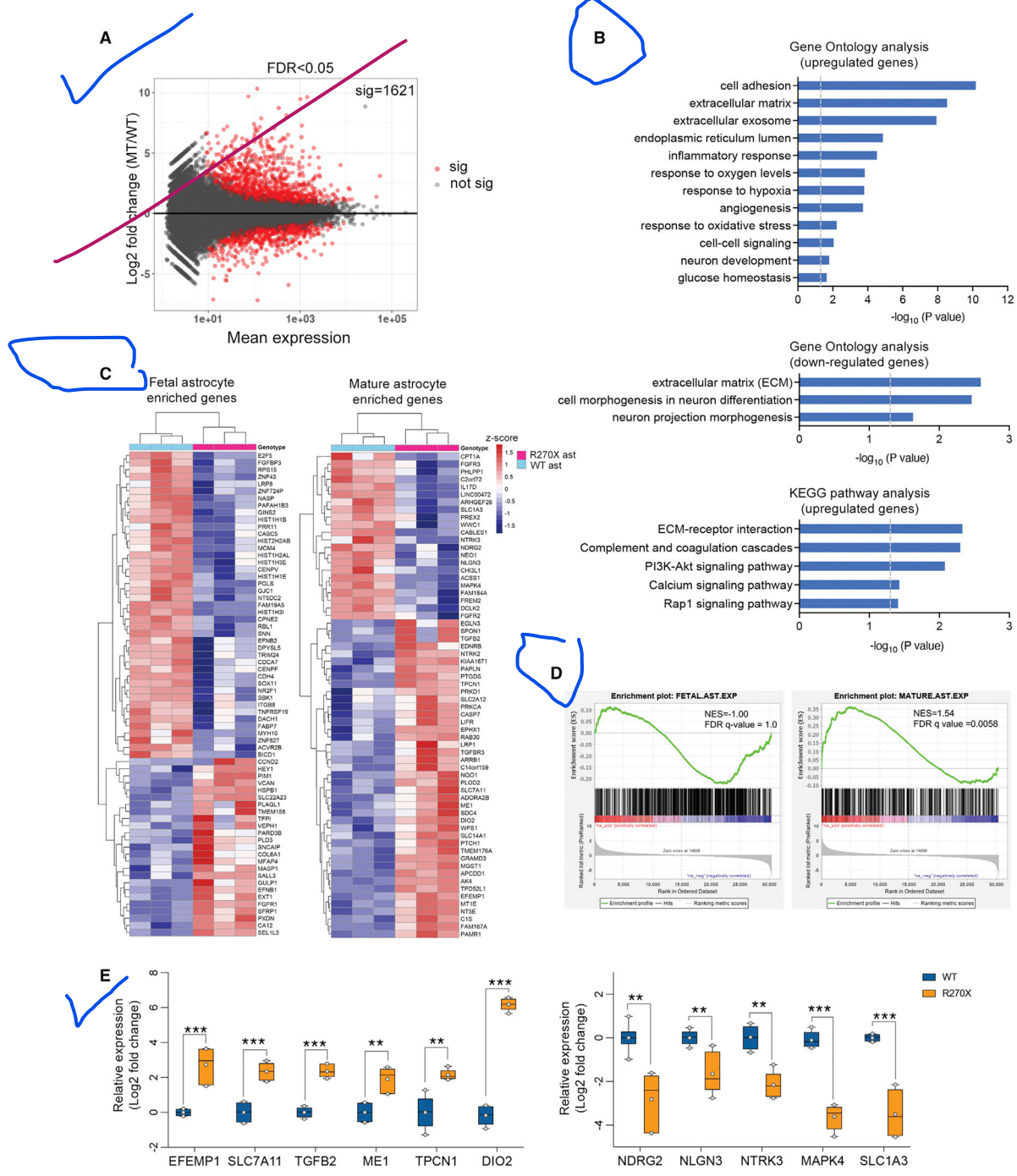


**Figure 2. Human astrocytes with R270X mutation in *MECP2* have altered transcriptome**  
 (A) MA plot shows differentially expressed genes between R270X mutant (MT) and WT astrocytes (false discovery rate [FDR] of <0.05). Red, significant differences(sig); gray, not significant differences (not sig).  
 (B) DAVID GO analysis for up-regulated (upper) and down-regulated (middle) genes and KEGG pathway analysis (bottom) for up-regulated genes in MT astrocytes. Vertical dashed line marks  $-\log_{10}(0.05)$ .

- (C) Heatmaps show significantly dysregulated fetal and mature astrocyte-enriched genes in MT astrocytes. Color legend shows Z score (STAR Methods).
- (D) Gene set enrichment analysis of fetal (left) and mature (right) astrocyte-enriched genes indicates significantly more up-regulated than down-regulated mature astrocyte-enriched genes (FDR qval of 0.0058) in the MT astrocytes (STAR Methods).
- (E) Quantitative reverse transcriptase PCR validation for selected dysregulated mature astrocyte-enriched genes. n = 3 biological replicates. Data represent mean ± standard error of the mean. Paired Student's t test. \*\* $p < 0.01$ , \*\*\* $p < 0.001$ . See also Figure S2; Tables S1, S2, and S3.

Author Manuscript

Author Manuscript

Author Manuscript

Author Manuscript

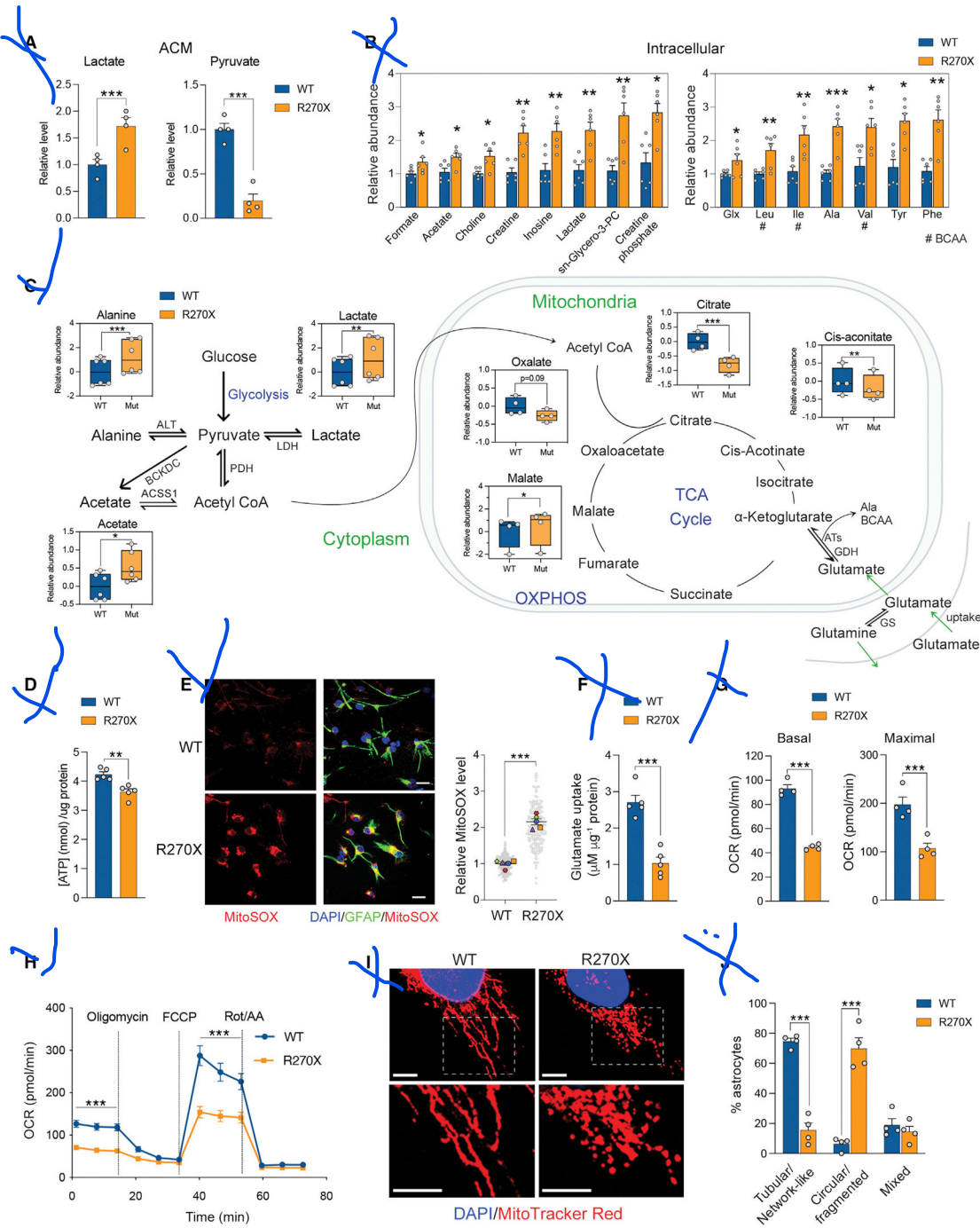


**Figure 3. Human astrocytes with R270X MECP2 mutation have altered energy metabolism and impaired mitochondrial structure and function**

(A) Quantitative  $^1\text{H}$  NMR of lactate and pyruvate levels in mutant and WT ACM. n = 4 biological replicates.

(B) Altered intracellular metabolites in mutant astrocytes based on  $^1\text{H}$  NMR. #, branched-chain amino acids (BCAA). Glx, glutamine/glutamate. n = 6 biological replicates.

(C)  $^1\text{H}$  NMR and targeted LC-MS/MS analysis show relative abundance (log2 scale) of intracellular metabolites related to glycolysis pathway and TCA cycle. n = 6 and 4 biological replicates for  $^1\text{H}$  NMR and targeted LC-MS/MS analyses, respectively.

- (D) ATP levels in mutant compared with WT astrocytes. n = 5 biological replicates.
- (E) Representative images of MitoSOX staining of mutant and WT astrocytes (left) and single-cell MitoSOX intensity quantification (right). n = 5 biological replicates, with the average of each represented by a data point in a separate color and shape. Gray data points represent MitoSOX intensity in individual cells; 33–40 cells per group per replicate. Scale bars, 50  $\mu$ m.
- (F) Glutamate uptake in mutant and WT astrocytes. n = 5 biological replicates.
- (G and H) Seahorse analysis of oxygen consumption in mutant and WT astrocytes, at baseline, and after treatment with oligomycin, FCCP (maximal respiration), and rotenone antimycin A (Rot/AA). n = 4 biological replicates, 8 technical replicates per group per replicate.
- (I and J) Representative images of MitoTracker Red staining (I) and quantification of aberrant mitochondrial structure in mutant versus WT astrocytes (J) (STAR Methods). Scale bars, 25  $\mu$ m. n = 4 biological replicates, data points represent average percentage of cells with specific mitochondrial structure in each biological replicate; total of 85 WT and 77 mutant astrocytes quantified. Data represent mean  $\pm$  standard error of the mean. Paired Student's t test. \*p < 0.05, \*\*p < 0.01, \*\*\*p < 0.001. See also Figures S3 and S4; Table S3. CoA, co-enzyme A.

Author Manuscript

Author Manuscript

Author Manuscript

Author Manuscript

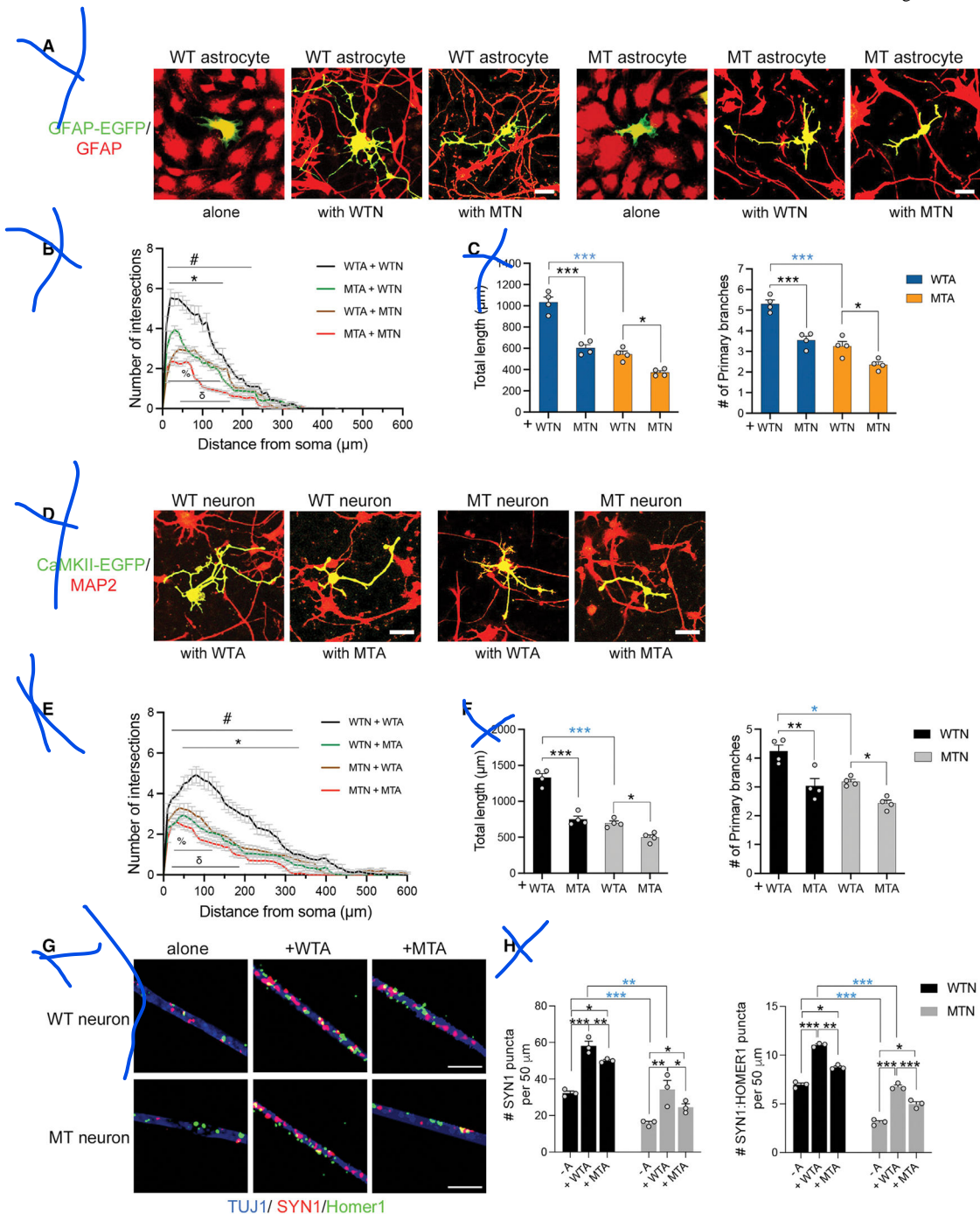


**Figure 4. Neuron-astrocyte co-cultures show cell- and non-cell-autonomous effects of R270X MECP2 mutation on astrocyte and neuron morphology**

(A) Representative images of GFAP-EGFP/GFAP labeled WT astrocytes (WTA) (left) and mutant astrocytes (MTA) (right), when cultured alone, with WT neurons (WTN), or with mutant neurons (MTN). The GFAP-EGFP<sup>+</sup>/GFAP<sup>+</sup> cells are MAP2 negative (not shown). (B and C) Sholl analysis (B) and quantification of primary branches and total length (C) of WT and mutant astrocytes when co-cultured with WTN or MTN. The symbols in (B) represent significant ( $p < 0.05$ ) differences in astrocyte morphology when different combinations of co-cultures are compared: #WTA-WTN versus MTA-WTN, \*WTA-WTN

versus WTA-MTN, %MTA-WTN versus MTA-MTN, and 8WTA-MTN versus MTA-MTN. Black asterisks in (C), significant non-cell-autonomous effect of MTN on astrocyte morphology; blue asterisks, significant cell-autonomous effect of *MECP2* mutation on MTA morphology.

(D) Representative images of CaMKII-EGFP/MAP2-labeled WT and MT neurons when co-cultured with WTA or MTa. The CaMKII-EGFP<sup>+</sup>/MAP2<sup>+</sup> cells are GFAP negative (not shown).

(E and F) Sholl analysis (E) and quantification of primary branches and total length (F) of WT and MT neurons when co-cultured with WTA or MTa. The symbols in (E) represent significant ( $p < 0.05$ ) differences in neuron morphology when different combinations of co-cultures are compared: #WTN-WTA versus WTN-MTA, \*WTN-WTA versus MTN-WTA, %WTN-MTA versus MTN-MTA, and 8MTN-WTA versus MTN-MTA. Black asterisks in (F), significant negative non-cell-autonomous effect of MTa on neuronal morphology; blue asterisks, significant cell-autonomous effect of *MECP2* mutation on MTN morphology. n = 4 biological replicates, 14–25 cells per group per replicate (B, C, E, F).

(G) Representative images of SYN1 and Homer1 synaptic puncta along TUJ1 processes in WT and mutant neurons, when cultured alone or co-cultured with WTA or MTa.

(H) Quantification of SYN1 puncta (left) and co-localized SYN1/Homer1 puncta (right) density along TUJ1 processes. Black asterisks, significant non-cell-autonomous effect of WTA and MTa on synapse formation; blue asterisks, significant cell-autonomous effect of *MECP2* mutation in neurons on synapse formation. n = 3 independent experiments, 5–7 fields quantified per group per experiment. Scale bars, 50 μm (A, D); 5 μm (G).

Data represent mean ± standard error of the mean. Two-way ANOVA with Tukey multiple comparison tests was used to determine differences between groups (B, C, E, F, H). \* $p < 0.05$ , \*\* $p < 0.01$ , \*\*\* $p < 0.001$ . See also Figures S5 and S6.

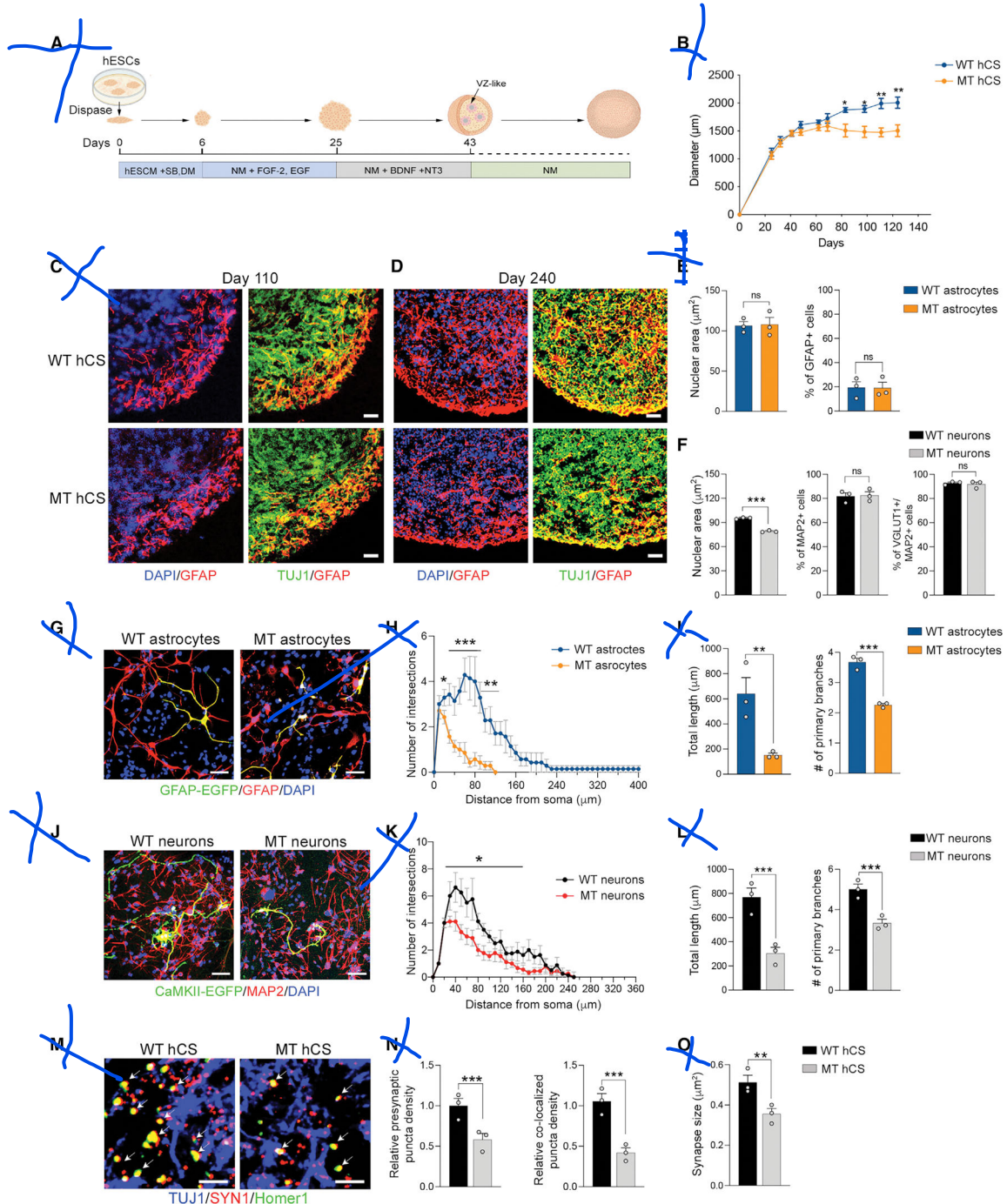


**Figure 5. Mutant astrocytes and neurons generated in hCSs are structurally compromised**  
(A) Diagram for hCS generation (STAR Methods).

(B) Growth rate of R270X mutant (MT) and WT hCSs.  $n = 14$  spheroids per group from two independent experiments.

(C and D) Immunostaining of WT and MT hCS cryosections at day 110 (C) and day 240 (D) show the presence of astrocytes (GFAP) and neurons (TUJ1).

(E–L) Analysis of dissociated MT and WT hCS cultures (days 180–200).

(E) Nuclear areas of astrocytes (left). Percentage of GFAP<sup>+</sup> astrocytes (right).

(F) Nuclear areas of neurons (left). Percentage of MAP2+ neurons (middle) and of VGlu + neurons among MAP2+ neurons (right). n = 3 biological replicates, 30–35 cells per group per replicate for nuclear size (E, F), 3–5 fields per group per replicate for percentage of cell types (E, F).

(G) Confocal images of GFAP-EGFP<sup>+</sup>/GFAP<sup>+</sup> astrocytes.

(H and I) Sholl analysis (H) and quantification of primary branches and total length (I) of GFAP-EGFP-traced MT and WT astrocytes.

(J) Images of CaMKII-EGFP<sup>+</sup>/MAP2<sup>+</sup> neurons.

(K and L) Sholl analysis (K) and quantification of primary branches and total length (L) of CaMKII-EGFP-traced MT and WT neurons. n = 3 biological replicates, 12–14 GFAP-EGFP<sup>+</sup> and 12–16 CaMKII-EGFP<sup>+</sup> cells per group per replicate (H, I, K, L).

(M) Immunostaining of hCS sections (day 110) for SYN1 and Homer1 synaptic puncta and the pan-neuronal marker TUJ1.

(N and O) The relative density of SYN1 and co-localized SYN1/Homer1 (N) synaptic puncta, and the size of SYN1 puncta (O), in MT compared with WT hCSs. n = 3 biological replicates, three hCSs per group per replicate, two to three cryosections per spheroid. Data represent mean ± standard error of the mean. Unpaired Student's t test. ns, not significant.

\*p < 0.05, \*\*p < 0.01, \*\*\*p < 0.001. Scale bars are 50 μm (C, D, G, J); 5 μm (M). See also Figure S7.

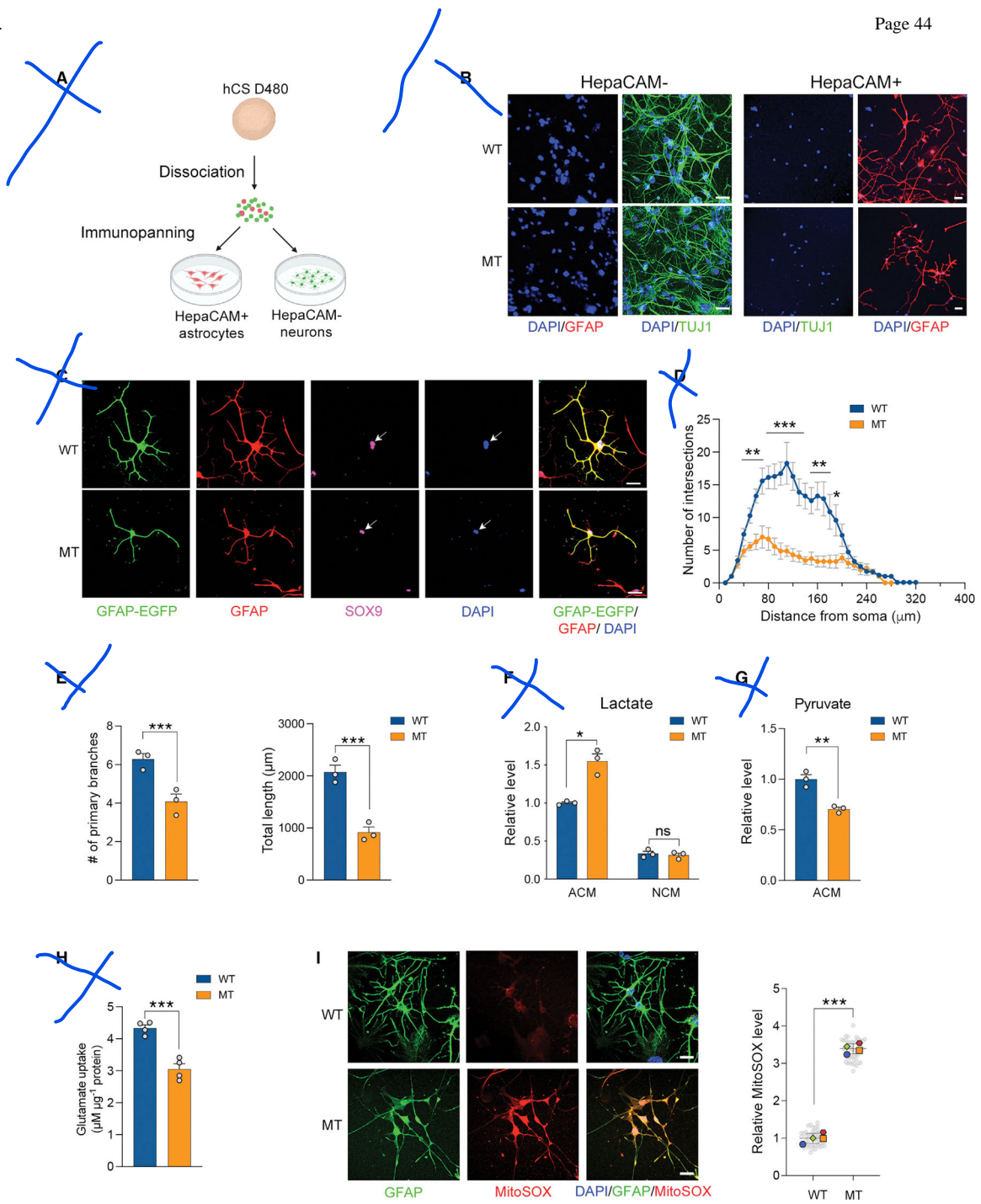


**Figure 6. Mutant human astrocytes generated and matured in long-term cortical spheroids show morphological and functional defects**

(A) Schematic for astrocyte immunopanning (STAR Methods).

(B) Images show highly enriched neuron ( $\text{TUJ1}^+$ ) and astrocyte ( $\text{GFAP}^+$ ) cultures after immunopanning (day 480).

(C) Images of single immunopanned astrocytes transfected with GFAP-EGFP co-express GFAP and SOX9. Arrows point to nuclei (DAPI/SOX9).

(D and E) Sholl analysis (D) and quantification of primary branches and total length (E) of immunopanned mutant and WT astrocytes. n = 3 biological replicates, 30–34 GFAP-EGFP<sup>+</sup> astrocytes were traced per genotype per replicate.

(F and G) <sup>1</sup>H NMR of lactate and pyruvate levels in astrocyte- and neuron-conditioned media (ACM, NCM) generated from immunopanned cell cultures. n = 3 biological replicates.

(H) Glutamate uptake in immunopanned MT and WT astrocytes. n = 4 immunopanned astrocyte cultures from two hCS batches.

(I) Images (left) and quantification (right) of MitoSOX intensity in single immunopanned mutant and WT astrocytes. n = 4 independent cultures of immunopanned astrocytes from two hCS batches, 18–20 cells per genotype per culture. The average of each biological replicate is represented by data point in a separate color and shape. Gray data points represent MitoSOX intensity in individual cells. Data represent mean ± standard error of the mean. Student's t tests. \*p < 0.05, \*\*p < 0.01, \*\*\*p < 0.001. Scale bars, 50 μm (B, I); 100 μm (C). See also Figure S8.

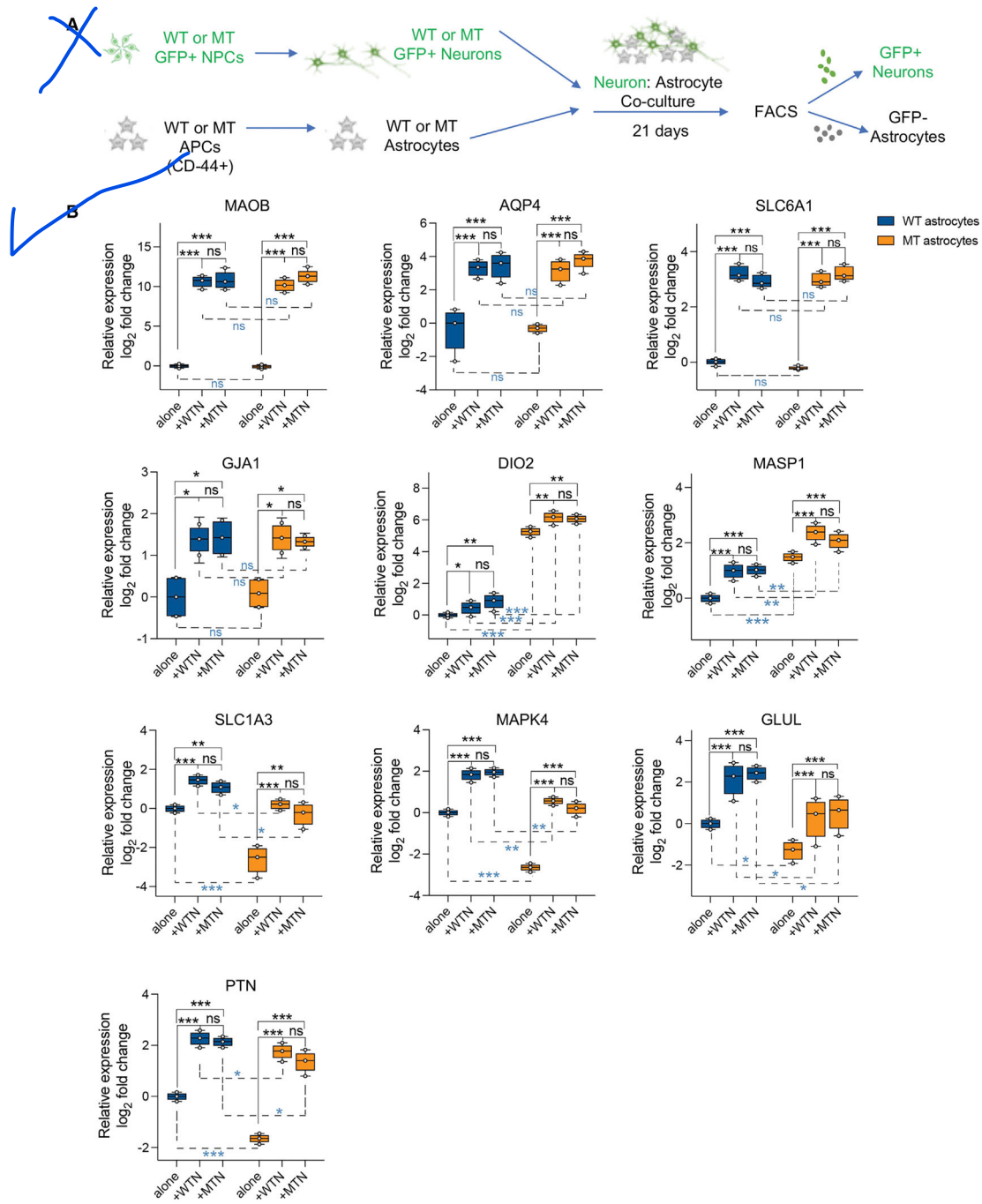


**Figure 7. Cell- and non-cell-autonomous effects of *MECP2* mutation on neuron-induced astrocyte gene expression**

(A) Schematic for neuron-astrocyte co-culture experiment (STAR Methods).

(B) Quantitative reverse transcriptase PCR shows relative expression of neuron-induced astrocyte genes in WT or R270X astrocytes (WTA, MTA) when cultured alone or co-cultured with WT or MT neurons (WTN, MTN) and then sorted. Black asterisks and solid lines, non-cell-autonomous effect of *MECP2* mutation in neurons on astrocyte gene expression. Blue asterisks and dashed lines, cell-autonomous effect of *MECP2* mutation on astrocyte gene expression. Comparisons performed between WTA and MTA cultured alone, and

between WTA and MTA co-cultured with WTN or MTN. n = 3 independent experiments. Bars represent mean  $\pm$  standard error of the mean. Two-way ANOVA with Tukey post hoc tests. \*p < 0.05, \*\*p < 0.01, \*\*\*p < 0.001. See also Figures S9.

### KEY RESOURCES TABLE

REAGENT or RESOURCE	SOURCE	IDENTIFIER
<b>Antibodies</b>		
Mouse anti-CD44	Abcam	Cat#: AB6124; RRID: AB_305297
Mouse anti-CD44-FITC	BD Biosciences	Cat#: 560977; RRID: AB_10563909
Goat anti-SOX2	Santa Cruz	Cat#: SC17320; RRID: AB_2286684
Goat anti-NANOG	R&D Systems	Cat#: AF2729; RRID: AB_2150103
Mouse anti-OCT3/4	Santa Cruz	Cat#: sc-5279; RRID: AB_628051
Goat anti-SOX1	R&D Systems	Cat#: AF3369; RRID: AB_2239879
Rabbit anti-PAX6	GeneTex	Cat#: GTX55739; RRID: AB_2894826
Mouse anti-Nestin	Millipore	Cat#: MAB353; RRID: AB_94911
Mouse anti-Ki67	BD Biosciences	Cat#: 550609; RRID: AB_393778
Rabbit anti-MeCP2	Cell Signaling	Cat#: 3456; RRID: AB_2143849
Mouse anti-S100B	Sigma-Aldrich	Cat#: S2532; RRID: AB_477499
Rabbit anti-GFAP	Millipore	Cat#: MAB5804; RRID: AB_2109645
Goat anti-Vimentin	R&D Systems	Cat#: AF2105; RRID: AB_355153
Mouse anti-human GFAP	Biolegend	Cat#: SMI21R; RRID: AB_509979
Goat anti-SOX9	R&D Systems	Cat#: AF3075; RRID: AB_2194160
Chicken anti-TUJ1	Aves	Cat#: TUJ; RRID: AB_2313564
Mouse anti-MAP2	Millipore	Cat#: MAB3418; RRID: AB_94856
Chicken anti-EGFP	Millipore	Cat#: AB16901; RRID: AB_11212200
Rabbit anti-SYN1 (Synapsin 1)	Abcam	Cat#: AB8; RRID: AB_2200097
Mouse anti-Homer1	Synaptic Systems	Cat#: 160011; RRID: AB_2120992
Mouse anti-human nuclei	Millipore	Cat#: MAB1281; RRID: AB_94090
Rabbit anti-CTIP2	Abcam	Cat#: Ab28448; RRID: AB_1140055
Mouse anti-HepaCAM	R&D Systems	Cat#: MAB4108; RRID: AB_2117687
Rabbit anti-Cleaved Caspase-3	Cell Signaling	Cat#: 9661S; RRID: AB_2341188
Rabbit anti-VGLUT1	Synaptic Systems	Cat#: 135302; RRID: AB_887877
Alexa Fluor 633 Goat anti-mouse	Thermo Fisher Scientific	Cat#: A21050; RRID: AB_141431
Alexa Fluor 546 Goat anti-rabbit	Thermo Fisher Scientific	Cat#: A11035; RRID: AB_143051
Alexa Fluor 488 Goat anti-chicken	Thermo Fisher Scientific	Cat#: A11039; RRID: AB_142924
Alexa Fluor 546 Donkey anti-goat	Thermo Fisher Scientific	Cat#: A11056; RRID: AB_142628
Alexa Fluor 488 Goat anti-rabbit	Thermo Fisher Scientific	Cat#: A11008; RRID: AB_143165
Cy-2 Donkey anti-chicken IgG	Jackson ImmunoResearch	Cat#: 703-225-155; RRID: AB_2340370
Cy-3 Donkey anti-rabbit IgG	Jackson ImmunoResearch	Cat#: 711-165-152; RRID: AB_2307443
Cy-5 Donkey anti-rabbit IgG	Jackson ImmunoResearch	Cat#: 711-175-152; RRID: AB_2340607
Cy-3 Donkey anti-mouse IgG	Jackson ImmunoResearch	Cat#: 715-165-151; RRID: AB_2315777
Cy-5 Donkey anti-mouse IgG	Jackson ImmunoResearch	Cat#: 715-175-151; RRID: AB_2619678
<b>Biological samples</b>		
Postmortem brain tissues of normal individuals and Rett syndrome patients	University of Maryland Brain & Tissue Bank	See Table S5 for details

REAGENT or RESOURCE	SOURCE	IDENTIFIER
Antibodies		
Chemicals, peptides, and recombinant proteins		
mTeSR1	STEMCELL Technologies	Cat#: 85850
Gentle Dissociation Reagent	STEMCELL Technologies	Cat#: 100–0485
DMEM-F12	Thermo Fisher Scientific	Cat#: 11330032
KnockOut Serum Replacement	Thermo Fisher Scientific	Cat#: 10828010
NEAA	Thermo Fisher Scientific	Cat#: 1140050
GlutaMAX	Thermo Fisher Scientific	Cat#: 35050061
β-mercaptoethanol	Sigma-Aldrich	Cat#: M3148
Penicillin/Streptomycin	Thermo Fisher Scientific	Cat#: 15070063
SB431542 (SB)	Abcam	Cat#: AB120163
Dorsomorphin (DM)	Tocris	Cat#: 3096
N-2	Thermo Fisher Scientific	Cat#: 17502048
B-27	Thermo Fisher Scientific	Cat#: 12587010
FGF-2 (bFGF)	Peprotech	Cat#: 100–18B
EGF	Peprotech	Cat#: 100–47
BMP4	Peprotech	Cat#: 120–05ET
CNTF	Peprotech	Cat#: 450–13
LIF	Peprotech	Cat#: 300–05
FGF-1	Peprotech	Cat#: 100–17A
Poly-L-ornithine	Sigma-Aldrich	Cat#: P4957
Laminin	Corning	Cat#: 354232
BrainPhys Neuronal Medium	STEMCELL Technologies	Cat#: 05790
Ascorbic Acid	Sigma-Aldrich	Cat#: A0278
BDNF	Peprotech	Cat#: 450–02
GDNF	Peprotech	Cat#: 450–10
NT3	Peprotech	Cat#: 450–03
HB-EGF	Peprotech	Cat#: 100–47
Dibutyryl-cAMP	Sigma-Aldrich	Cat#: D0627
Matrigel	BD Biosciences	Cat#: 1385
CHIR 99021	Axon Medchem	Cat#: 356234
Purmorphamine (PMA)	Alexis	Cat#: ALX-420-045-M001
Neural Rosette Selection Reagent	STEMCELL Technologies	Cat#: 05832
EGF	R&D Systems	Cat#: 236-EG-200
hLIF	Peprotech	Cat#: 300–05
Accutase	Thermo Fisher Scientific	Cat#: A1110501
Vectashield antifade mounting medium containing DAPI	Vector s	Cat#: H-1200-10
TransIT-293 transfection reagent	Mirus Bio	Cat#: MIR 2704
TRIzol	Thermo Fisher Scientific	Cat#: 15596026
CalPhos™ Mammalian Transfection Kit	Takara	Cat#: 631312
TransIT-2020 transfection reagent	Mirus Bio	Cat#: MIR 5404

REAGENT or RESOURCE	SOURCE	IDENTIFIER
Dispase	Millipore Sigma	Cat#: SCM133
Neurobasal-A medium	Thermo Fisher Scientific	Cat#: 10888
Hoechst 33258	Thermo Fisher Scientific	Cat#: H3569
Papain	Worthington	Cat#: 9001-73-4
Soybean protease inhibitor	Thermo Fisher Scientific	Cat#: 17075-029
Ovomucoid protease inhibitor	Worthington	Cat#: 9035-81-1
<hr/>		
Critical commercial assays		
miRNeasy Mini Kit	Qiagen	Cat#: 217084
SYBR green PCR master mix	Thermo Fisher Scientific	Cat#: 4309155
Amplex Red Glutamic Acid/Glutamate Oxidase Assay Kit	Thermo Fisher Scientific	Cat#: A12221
Pierce BCA protein assay	Thermo Fisher Scientific	Cat#: 23225
ATP Bioluminescence Assay Kit	PerkinElmer	Cat#: 6016943
MitoSOX Red	Thermo Fisher Scientific	Cat#: M36008
Seahorse XF Mito Stress kit	Agilent	Cat#: 103015-100
MitoTracker Green FM	Thermo Fisher Scientific	Cat#: M7514
MitoTracker Red CMXRos	Thermo Fisher Scientific	Cat#: M7512
<hr/>		
Deposited data		
RNA sequencing data	This paper	GEO: GSE185726
<hr/>		
Experimental models: Cell lines		
H1 hESC line	WiCell	N/A
H1-MeCP2-R270X	Xiang et al. <sup>23</sup>	N/A
H1-MeCP2-R133C	Xiang et al. <sup>23</sup>	N/A
<hr/>		
Experimental models: Organisms/strains		
B6.129S7-Rag1tm1Mom/J	The Jackson Laboratory	Cat#: 002216
<hr/>		
Oligonucleotides		
Primers used for RT-qPCR	Integrated DNA Technologies	Table S4
Primer MECP2-R133C Forward (DNA seq)	Integrated DNA Technologies	ACATCAGAAGGGTCAGGCTC
Primer MECP2-R133C Reverse (DNA seq)	Integrated DNA Technologies	GCTCCATGAGGGATCCTTGT
Primer MECP2-R270X Forward (DNA seq)	Integrated DNA Technologies	CCTTTCAAACCTGCCAGGG
Primer MECP2-R270X Reverse (DNA seq)	Integrated DNA Technologies	GTACGGTCTCCTGCACAGAT
<hr/>		
Recombinant DNA		
Plasmid FUGW (UbiquitinC-EGFP)	David Baltimore lab	N/A
Plasmids VSV-G	Didier Trono lab	N/A
Plasmid CMV- 8.9	Didier Trono lab	N/A
Plasmid FCK(1.3)GW (CaMKII-EGFP)	Pavel Osten lab	N/A

REAGENT or RESOURCE	SOURCE	IDENTIFIER
Antibodies		
Plasmid LV-hGFAP-EGFP	Chun-Li Zhang lab	N/A
Software and algorithms		
ImageJ	NIH	<a href="https://imagej.nih.gov/ij/">https://imagej.nih.gov/ij/</a>
GraphPad Prism 9.0	Graphpad	<a href="https://www.graphpad.com/scientific-software/prism/">https://www.graphpad.com/scientific-software/prism/</a>
DAVID gene ontology Bioinformatics Resources	LHRI	<a href="https://david.ncifcrf.gov/">https://david.ncifcrf.gov/</a>
Chenomx NMR Analysis Software	Chenomx	<a href="https://www.chenomx.com/">https://www.chenomx.com/</a>
MassHunter Quantitative Analysis	Agilent	<a href="https://www.agilent.com/">https://www.agilent.com/</a>
Neurolucida 360	MBF Bioscience	<a href="https://www.mbfbioscience.com/products/neurolucida-360">https://www.mbfbioscience.com/products/neurolucida-360</a>
BioRender	BioRender	<a href="http://Biorender.com">http://Biorender.com</a>
Wave	Agilent	<a href="https://www.agilent.com/">https://www.agilent.com/</a>
Other		
FACSAria III cell sorter	BD Biosciences	N/A
ABI StepOnePlus real-time PCR system	Thermo Fisher Scientific	N/A
NovaSeq 6000 Sequencing System	Illumina	N/A
Bruker 800 MHz AVANCE III NMR spectrometer	Bruker	N/A
Seahorse extracellular flux analyzer	Agilent	N/A
FilterMax plate reader	Molecular Devices	N/A
Leica TCS- SP5 microscope	Leica	N/A